

Numerical Investigation of Neutral and Unstable Planetary Boundary Layers

JAMES W. DEARDORFF

National Center for Atmospheric Research,¹ Boulder, Colo. 80302

(Manuscript received 8 July 1971)

ABSTRACT

Results of numerical integrations are presented for a neutrally stratified planetary boundary layer containing a passive scalar, and for three unstable cases with upward heat flux. The air is assumed unsaturated. A total of either 16,000 or 32,000 grid points was used in a three-dimensional region with length and width several times the height of the boundary layer. A key result is the irrelevance of the neutral height scale, u_*/f , and its replacement by the height z_i of the inversion base which confines the convective mixing when $-z_i/L$ is as small as 1.5 (L is the Monin-Obukhov length). Shapes of the eddies are examined for $-z_i/L = 0, 1.5, 4.5$ and 45 ; and only for the two slightly unstable cases were the vertical velocity eddies distinctly elongated as in Ekman-layer theories. At large instabilities it is shown how the friction velocity u_* loses its influence upon the turbulence intensities and a convective velocity scale becomes important.

Vertical profiles of mean wind, potential temperature, momentum flux, gross eddy coefficients, flux correlation coefficients, turbulence intensities, temperature variance and pressure fluctuations are presented and compared, when possible, with measurements. Comparison is hindered by the lack of observations of z_i and L in almost all field studies. Various terms in the turbulence kinetic energy equation, which are difficult to measure, are discussed quantitatively.

The rate at which particles released near the surface are transported vertically by the calculated turbulence is found from Lagrangian integrations to be up to two orders of magnitude greater in unstable cases than in a typical neutral case.

1. Introduction

By means of three-dimensional numerical modeling, it now appears possible to determine the structure and related statistics of energy-containing eddies within most of the planetary boundary layer (PBL). This was done with a minimum of numerical resolution by Deardorff (1970a), to be referred to as D1, for the idealized, neutral case (no vertical flux of heat). Results from a model encompassing a larger horizontal area but with equal resolution were reported for unstable cases (upward heat flux) only in briefest detail (Deardorff, 1970b, c). The purpose of this paper is to present more complete results for these unstable cases, and to make comparisons with new results for the neutral case which utilized the enlarged numerical model and contained a passive scalar.

Evidence will be presented in support of the following conclusions:

1) With even a very small upward heat flux, the appropriate stability parameter under equilibrium conditions is $-z_i/L$, where z_i is the height (above the surface) of the inversion base below which the convective mixing is confined, and L is the Monin-Obukhov length. In contrast, Clarke (1970) used the parameter $u_*/(fL)$, where u_* is the friction velocity based on the

surface wind stress, and f the magnitude of the Coriolis parameter.

2) The heights of the unstable PBL's for heat and momentum are nearly the same, and given approximately by z_i rather than by some fraction of u_*/f . As has been discussed by Lilly (1968), the length $|L|$ acts as an upper bound to the height at which the turbulence is strongly influenced by surface shear. Since $-L$ is not often greater than 100 m, the friction velocity u_* which appears in L can have no influence in maintaining a mixed layer of perhaps 1 km thickness. Therefore, neither can u_*/f determine the height of the unstable PBL. In contrast, Monin (1970) and Tennekes (1970) have assumed that the height of the momentum boundary layer, at least, remains proportional to u_*/f in unstable conditions.

3) In the neutral case, the eddies of both the downstream velocity component (u) and a passive scalar (θ) having a distributed surface flux are distinctly elongated near the surface in the direction of the shear at low levels, and are remarkable well correlated with each other. The structure resembles that of Ekman instability theories which assume two-dimensionality. However, the occurrence of three-dimensional turbulence essentially masks the elongation in structure of the vertical velocity component (w), and no such elongation or two-dimensionality appears at all in the structure of the pressure fluctuation.

¹ The National Center for Atmospheric Research is sponsored by the National Science Foundation.

4) For $-z_i/L=1.5$, the w eddies are similarly elongated because of the correlation of w with temperature in addition to its negative correlation with u . With $-z_i/L=4.5$, this elongation of the u , w and temperature eddies is along the direction of the surface wind.

5) For $-z_i/L$ of order 4.5 or more, the rms vertical velocity scales in magnitude with the convective velocity scale w_* (Deardorff, 1970c) and the temperature fluctuations with the temperature scale T_* (which equals the surface kinematic heat flux divided by w_*).

6) With $-z_i/L$ of order 45 and more, the large-scale structure is one of free convection with no preferred horizontal eddy orientation above a small height comparable to $-L$.

7) The time necessary for particles released simultaneously from a plane near the surface to become well mixed vertically throughout the PBL is typically one to two orders of magnitude longer in the neutral case than in the unstable case. In the latter case this time is about $1.6z_i/w_*$.

2. The numerical model and governing equations

a. Region treated

The domain extended to a height of $h=z_i$ in unstable cases, where a lid was imposed in crude simulation of an inversion base. In the neutral case the height h corresponded to $0.45u_*/f$ in one numerical integration, and to $1.0u_*/f$ in another. The first of these two neutral cases will receive more emphasis here because the resolution was then better in the region of strongest turbulence.

The length treated in the downstream (x) direction (at the surface) was $4h$. In the cross-stream (y) direction the width was $2h$ for the cases $-z_i/L=0$ and 4.5, and $4h$ for the two other cases treated with $-z_i/L=1.5$ and 45. This region was translated downstream at a constant velocity (nearly equal to the vertically integrated mean velocity) through a simple Galilean transformation.

The region was split into 40 grid intervals along x , 20 along y (except 40 for the cases $-z_i/L=1.5$ and 45), and 20 along the vertical z direction.

b. Small-scale Reynolds averaging

The governing equations were considered to have been averaged continuously in space over a volume equal to the grid volume $\Delta x \Delta y \Delta z$. A calculated variable centered at some grid point then represents the average over the surrounding grid volume, so that finite-difference equations can be used as fair approximations to the true differential equations without excessive truncation error. That is, the Reynolds-averaged dependent variables varied rather smoothly in space and time because of the use of a positive sub-grid-scale (SGS) eddy coefficient in representing the SGS Reynolds stresses.

Following the method of Lilly (1967), the error due to lack of validity of Reynolds averaging assumptions can be combined with uncertainties in the assumption for the Reynolds stresses (to be discussed later) and does not require separate assumption or discussion.

c. The governing equations

After Reynolds averaging, and after making lengths dimensionless by h , velocities by u_* , and time by h/u_* , the equations of motion with the Boussinesq assumption become

$$\begin{aligned} \frac{\partial u_i}{\partial t} = & -\frac{\partial}{\partial x_j} \left[\bar{u}_i \bar{u}_j - K_m \left(\frac{\partial \bar{u}_i}{\partial x_j} + \frac{\partial \bar{u}_j}{\partial x_i} \right) \right] \\ & + \left(\frac{2h\Omega_{i-1}}{u_*} \right) \bar{u}_{i+1} - \left(\frac{2h\Omega_{i+1}}{u_*} \right) \bar{u}_{i-1} \\ & - \delta_{i3} \frac{gh}{u_*^2} \left(\frac{\bar{\rho}}{\langle \bar{\rho} \rangle} - 1 \right) - \frac{\partial \langle \bar{P} \rangle}{\partial x_i} - \frac{\partial \bar{P}''}{\partial x_i}, \\ = & R_i - \partial \bar{P}'' / \partial x_i. \end{aligned} \quad (1)$$

The overbar denotes the grid-volume Reynolds average; subscripts i or $j=1, 2$ or 3 correspond to $x_1=x$, $x_2=y$ and $x_3=z$, respectively, with the summation convention used; K_m is the SGS eddy coefficient for momentum; Ω_i is the i th component of the earth's angular velocity; \bar{P} is the dimensionless pressure given by

$$\bar{P} = [\bar{p} / (\langle \bar{\rho} \rangle u_*^2)] + \frac{1}{3} \overline{u_j' u_j'} / 3, \quad (2)$$

where p is the static pressure, ρ the density and $\overline{u_j' u_j'}/3$ the average of the local normal SGS stress components; the angular brackets indicate the horizontal average over an area equal in size to that treated; the double prime denotes the deviation from the local value of the horizontal mean, i.e., $\bar{P}'' = \bar{P} - \langle \bar{P} \rangle$; and R_i is seen to be the entire right-hand side of the i th momentum equation except for the fluctuating pressure gradient.

The mean pressure gradients, $\partial \langle \bar{P} \rangle / \partial x$ and $\partial \langle \bar{P} \rangle / \partial y$, were assumed constant in space (no horizontal gradients of mean density, and rectilinear isobars) and were individually prescribed on each time step of the integration to have the values which would produce no acceleration of the fluid as a whole when the momentum-flux components at the surface equal their equilibrium values. The method here is the same as described in D1, except that if a non-zero component of the stress in the y direction occurred at the surface this was allowed for in the calculation of $\partial \langle \bar{P} \rangle / \partial y$.

In (1), Ω_1 was set equal to zero (west wind) and Ω_2 set equal to Ω_3 (45N). The model-height Rossby number, $u_*/(2h\Omega_3) = u_*/(hf)$, was set at 2.2 except for the case $-z_i/L=1.5$ for which it was set at unity. Previous integrations for the neutral case suggested that neither

the direction of the surface wind nor the latitude noticeably affect boundary layer turbulence except in the limiting equatorial case.

For $i=3$ in (1) the buoyancy term was rewritten in terms of a dimensionless potential temperature, and horizontal mean values removed, as follows:

$$\begin{aligned} \frac{\partial \bar{u}_3}{\partial t} &= -\frac{\partial}{\partial x_j} \langle \bar{u}_3 \bar{u}_j \rangle + \frac{\partial}{\partial x_3} \langle \bar{u}_3^2 \rangle \\ &\quad + \frac{\partial}{\partial x_j} \left[K_m \left(\frac{\partial \bar{u}_3}{\partial x_j} + \frac{\partial \bar{u}_j}{\partial x_3} \right) \right] - \frac{\partial}{\partial x_3} \left\langle 2K_m \frac{\partial \bar{u}_3}{\partial x_3} \right\rangle \\ &\quad + \frac{1}{k} \frac{h}{L} (\bar{\Theta} - \langle \bar{\Theta} \rangle) + \left(\frac{2h\Omega_2}{u_*} \right) (\bar{u}_1 - \langle \bar{u}_1 \rangle) \\ &\quad - \left(\frac{2h\Omega_1}{u_*} \right) (\bar{u}_2 - \langle \bar{u}_2 \rangle) - \frac{\partial \bar{P}''}{\partial x_3}, \\ &= R_3 - \partial \bar{P}'' / \partial x_3, \end{aligned} \quad (3)$$

where k is the von Kármán constant and $\bar{\Theta}$ the dimensionless temperature given by

$$\bar{\Theta} = (\bar{\theta}_v - \theta_{vs}) u_* / \langle -\bar{w} \theta_v \rangle_s. \quad (4)$$

In (4), θ_v is the virtual potential temperature, θ_{vs} its surface equilibrium value which is assumed constant in space, and $\langle \bar{w} \theta_v \rangle_s$ the kinematic flux of virtual potential temperature close to the surface and averaged over the horizontal. The caret is used when necessary to denote a dimensional variable. The use of θ_v allows the influence of water vapor upon buoyancy to be taken into account.

The Monin-Obukhov length L which appears in (3) is here defined for moist but unsaturated air by

$$L = -u_*^3 / \left(k \frac{g}{\theta_{vm}} \langle \bar{w} \theta_v \rangle_s \right),$$

where θ_{vm} is the mean value of θ_v throughout the PBL.

In (3), the dimensionless parameter containing the whole influence of thermal instability is h/L ; it equals z_i/L in unstable cases. If, therefore, the turbulence is then found to be confined in height by z_i rather than by some small fraction of u_*/f , this result would constitute evidence that z_i/L is the appropriate stability parameter in unstable cases.

If the horizontal average, $\langle \rangle$, is taken of (3), we see that the right-hand side is identically zero, giving $\partial \langle \bar{u}_3 \rangle / \partial t = 0$. That $\langle \bar{u}_3 \rangle$ should be zero initially and maintained zero follows from the horizontal average of the continuity equation

$$\partial \bar{u}_i / \partial x_i = 0 \quad (5)$$

above horizontal terrain, assuming large-scale horizontal homogeneity of the velocity components. The Poisson equation from which \bar{P}'' is obtained is thus

given by the finite-difference approximation of

$$\nabla^2 \bar{P}'' = \partial R_i / \partial x_i - \frac{\partial}{\partial t} \langle \bar{u}_i / \partial x_i \rangle. \quad (6)$$

The conservation equation for $\bar{\Theta}$, after SGS Reynolds averaging, is

$$\begin{aligned} \frac{\partial \bar{\Theta}}{\partial t} &= -\frac{\partial}{\partial x_j} \langle \bar{u}_j \bar{\Theta} \rangle - K_h \partial \bar{\Theta} / \partial x_j \\ &\quad + (\mathcal{R} - \partial \theta_{vs} / \partial t) z_i / \langle -\bar{w} \theta_v \rangle_s, \end{aligned} \quad (7)$$

where K_h is the SGS eddy coefficient for heat, \mathcal{R} a dimensional rate of temperature change associated with divergence of radiative flux, and $\partial \theta_{vs} / \partial t$ the rate at which the surface value of θ_v increases with dimensional time (t). The existence of this equation follows from 1) multiplication of the first law of thermodynamics, $d\theta/dt=0$, by $(1+0.61q_m)$, where q_m is a constant value of the specific humidity q nearly equal to the average value throughout the PBL; 2) multiplication of the equation $dq/dt=0$ by $0.61\theta_m$; and 3) addition of the two. The quantity $(1+0.61q_m)\theta + 0.61\theta_m q$ in the resulting conservation equation differs from $\theta_v = \theta(1+0.61q)$ only by the amount $0.61(\theta - \theta_m)(q - q_m)$, i.e., by about 1% at most. This use of θ_v does not necessarily imply good correlation between q and θ , nor similar boundary conditions for the two variables, nor similar spectra.

Since heat, in general, is continually being fed into the air from the surface in this problem and none leaves the level $\hat{z}=z_i$, the virtual potential temperature itself cannot attain an equilibrium profile. However, $\bar{\Theta}$ in (4) depends upon $\bar{\theta}_v - \theta_{vs}$, so that $\langle \bar{\Theta} \rangle$ can indeed achieve an equilibrium profile if θ_{vs} increases with time along with $\bar{\theta}_v$. This requires the last term in (7) to balance the vertical convergence of the turbulent heat flux. The condition for this balance, from (7), is

$$\left(\mathcal{R} - \frac{\partial \theta_{vs}}{\partial t} \right) \frac{z_i}{\langle -\bar{w} \theta_v \rangle_s} = \frac{\partial}{\partial z} \langle \bar{w} \bar{\Theta} \rangle \equiv \frac{\partial}{\partial z} \left\langle \bar{w} \bar{\Theta} - K_h \frac{\partial \bar{\Theta}}{\partial z} \right\rangle. \quad (8)$$

From (8), we see that either the terms on the left-hand side could be individually specified, or, equivalently, $\langle \bar{w} \bar{\Theta} \rangle$ could be specified. The latter procedure was employed so that a realistic heat-flux profile would be achieved. The assumed profile is

$$\langle -\bar{w} \bar{\Theta} \rangle = (1-z)^2, \quad (9)$$

and is shown in Fig. 1. A linear profile is also shown and would occur if \mathcal{R} were constant with height. The profile assumed for $\langle -\bar{w} \bar{\Theta} \rangle$ is seen to be a compromise between a linear one and that measured by Lenschow (1970), and designed to give zero heat flux at $z=1$. The actual enthalpy flux must be negative at $z=1$ due

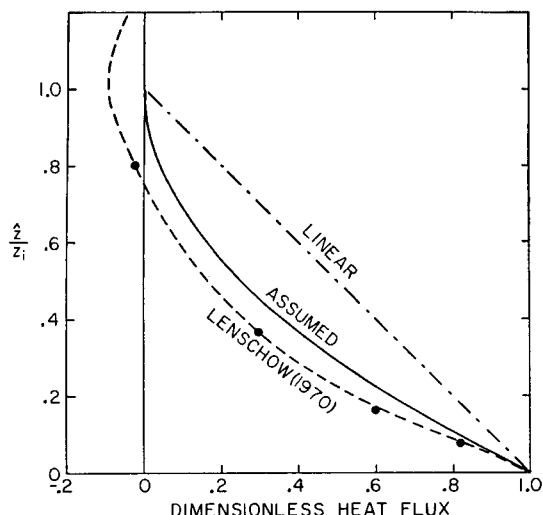


FIG. 1. Vertical profiles of heat flux, made dimensionless by its surface value. The solid curve was used in this study.

to downward entrainment of warm stable air into the convective region. However, this mechanism and the resulting tendency for z_i to increase with time were not modeled here. Instead, one could consider a peculiar distribution of \mathcal{Q} with height, beneath an infinitely strong inversion based at z_i , to be the cause of the curvature in the assumed profile of $\langle w\Theta \rangle$ in (9).

d. Sub-grid-scale eddy coefficients

The dimensionless K_m in (1) and (3) was prescribed, after the manner of Smagorinsky (1963), Lilly (1967) and Deardorff (1970d), by

$$K_m = (c\Delta)^2 \left[\frac{1}{2} \left(\frac{\partial \bar{u}_i}{\partial x_j} + \frac{\partial \bar{u}_j}{\partial x_i} \right) \left(\frac{\partial \bar{u}_i}{\partial x_j} + \frac{\partial \bar{u}_j}{\partial x_i} \right) \right]^{\frac{1}{2}}, \quad (10)$$

where $\Delta = (\Delta x \Delta y \Delta z)^{\frac{1}{3}}$, and c is a constant whose value is discussed in Deardorff (1971). It was set equal to 0.21 in the unstable cases and to 0.13 in the neutral case, except at the lowest grid level at $z = \frac{1}{2}\Delta z$. There the value of ~ 0.10 was used in all cases, which is the approximate value to be expected in the law-of-the-wall region for the grid mesh utilized if most of the shear stress there is carried by SGS eddies.

The change in c from 0.21 in unstable cases to 0.13 in the neutral case was due to the much greater mean shear in the latter case which enters into the velocity deformation in (10). However, it now appears, in the derivation of (10), that any large-scale mean flow, such as that which obtains its energy from a constant pressure gradient, should be removed from the velocity deformation utilized in the K_m formulation. This conclusion stems from the belief that K_m should be related dimensionally to the grid interval and to the local rate of dissipation of turbulence energy, $\bar{\epsilon}$, rather than to the

rate of degradation of total energy. To derive an approximate expression for $\bar{\epsilon}$, one subtracts the $\langle \cdot \rangle$ average of the i th equation of motion for \bar{u}_i from the latter equation before multiplying by \bar{u}_i'' to form a kinetic energy equation. The expression for K_m which emerges is essentially that given by (10) but with \bar{u}_i replaced by \bar{u}_i'' . This modification to (10) was tested for the neutral case after completion of the present study, and it was found that $c=0.21$ is then appropriate whether or not there is significant mean shear in the interior. Next to the surface a slightly larger value of c (about 0.23 or 0.24) was then needed for compatibility with surface-layer K_m formulations. No difference in the turbulence patterns or statistics was detected, in comparison with the results to be presented for the neutral case, which could be attributed to the revised formulation for K_m .

In (7), K_h was set equal to

$$K_h = 3K_m, \quad (11)$$

except in the neutral case studied first, where $K_h = 2K_m$ was tried. However, a factor appreciably smaller than 3 in (11) was found to lead to excessive intensity at the larger wavenumbers in the temperature spectrum at interior levels. At $z = \frac{1}{2}\Delta z$, a factor closer to unity was utilized to be compatible with the surface-layer formulations of Businger *et al.* (1966). At this level, the large-scale eddy coefficients formed from both calculated and SGS fluxes become nearly synonymous with the SGS eddy coefficients which become relatively large. At higher levels, however, the former eddy coefficients dominate and become nearly independent of the latter.

Lilly (private communication) suggests a ratio $K_h/K_m = 2.5$ on the grounds that the generation of a stress in an initially isotropic flow is reduced 60% by the pressure-velocity correlation (see Lilly, 1967, or Crow, 1968), while that of a scalar flux is not similarly affected. Completion of the argument requires that the time scales of relaxation of momentum and scalar fluxes be nearly identical.

The SGS fluxes in (1) and (7) are seen to have been expressed by

$$\overline{u_i' u_j'} - \frac{1}{3} \delta_{ij} \overline{u_n' u_n'} = -K_m (\partial \bar{u}_i / \partial x_j + \partial \bar{u}_j / \partial x_i), \quad (12)$$

$$\overline{u_i' \Theta'} = -K_h \partial \bar{\Theta} / \partial x_i. \quad (13)$$

The appearance of $\overline{u_n' u_n'}/3$ in (12) when $i=j$ explains the inclusion of the same quantity in the effective pressure \bar{P} in (2). This SGS energy needs to be estimated only for the purpose of adding it to the explicitly calculated kinetic energy to obtain the total turbulence energy. For this purpose, Lilly's (1967) formulation was used:

$$\overline{u_n' u_n'} = \frac{2}{3} K_m^2 / (0.09\Delta)^2, \quad n=1, 2, 3, \quad (14)$$

and it was further assumed that $\overline{u_1'^2} = \overline{u_2'^2} = \overline{u_3'^2}$. This latter assumption need not be made, however, and it would be possible to modify (12) so as to allow non-equipartition of SGS energy without violating the continuity equation.

For the SGS temperature variance, it was assumed that

$$\langle \overline{\Theta'^2} \rangle = [\langle \overline{\Theta''^2} \rangle / \langle \overline{u''^2} \rangle] \langle \overline{u'^2} \rangle. \quad (15)$$

The justification lies in the high correlation between \bar{u}'' and $\bar{\Theta}''$, to be discussed later, which is most pronounced near the surface where the SGS contribution is greatest.

e. Boundary conditions

At the vertical sides of the volume treated, cyclic boundary conditions were imposed upon \bar{u} , \bar{v} , \bar{w} , $\bar{\Theta}$ and \bar{P}'' .

At $z=1$, the conditions $\bar{w}=0$, and $\partial\bar{u}/\partial z = \partial\bar{v}/\partial z = \partial\bar{\Theta}/\partial z = 0$ were specified. Although these are logical conditions to impose at some level, it would be preferable (if computing power permitted) to impose them at a height considerably greater than z_i in unstable cases, and considerably higher than $0.45u_*^*/f$ in the neutral case. Also, $\partial\bar{\Theta}/\partial z$ could then be set to some standard value.

At $z=0$, \bar{w} was also set to zero. However, the conditions for \bar{u} , \bar{v} and $\bar{\Theta}$ were prescribed with respect to the second derivative in z at the level $z=\frac{1}{2}\Delta z$. This level is assumed to lie within the "constant-flux" region or the "law-of-the-wall" region, and the conditions imposed there were:

$$\left. \begin{aligned} \frac{\partial^2 \bar{u}}{\partial z^2} &= \frac{-F_1(\frac{1}{2}\Delta z/L)}{k(\Delta z/2)^2} + \frac{\partial^2 \bar{u}}{\partial y^2} \end{aligned} \right\} \quad (16)$$

$$\left. \begin{aligned} \frac{\partial^2 \bar{v}}{\partial z^2} &= \frac{\partial^2 \bar{v}}{\partial x^2} \end{aligned} \right\} z = \frac{1}{2}\Delta z \quad (17)$$

$$\left. \begin{aligned} \frac{\partial^2 \bar{\Theta}}{\partial z^2} &= \frac{-F_2(\frac{1}{2}\Delta z/L)}{k(\Delta z/2)^2} + \frac{\partial^2 \bar{\Theta}}{\partial y^2} \end{aligned} \right\} \quad (18)$$

where F_1 and F_2 are stability functions which are unity in the neutral case with mean profiles then being assumed logarithmic below $\frac{1}{2}\Delta z$, and are somewhat less than unity in unstable cases. In the latter cases, values of F_1 and F_2 were calculated from the surface-layer profile formulations of Businger (1966) and are given in Table 1. The last term on the right of (16)–(18) was imposed so that the second derivation in z would not simply be constant in the horizontal, and would contribute toward transfer of energy to the sub-grid-scale by means of the eddy-coefficient terms.

The last column in Table 1 gives the ratio of the SGS

TABLE 1. Values of F_1 and F_2 using data of Businger (1966).

$-z_i/L$	F_1	F_2	$(K_h/K_m)_{\frac{1}{2}\Delta z}$
0.	1.00	1.00	1.00
1.5	0.97	0.93	1.12
4.5	0.90	0.79	1.30
45	0.59	0.34	2.09

eddy coefficients utilized at $z=\frac{1}{2}\Delta z$; at higher levels (11) was used.

An additional boundary condition was imposed to cause $\partial\langle\bar{u}\rangle/\partial t$ and $\partial\langle\bar{\Theta}\rangle/\partial t$ to be zero at $z=\frac{1}{2}\Delta z$. Thus, $\langle\bar{u}\rangle$ and $\langle\bar{\Theta}\rangle$ could later be set to fixed values at this level, compatible with surface-layer formulations. This was accomplished, as described by Deardorff (1970d), by prescribing $\partial K_m/\partial z$ and $\partial K_h/\partial z$ centered at $z=0$ to be proportional to K_m and K_h , respectively, at $z=\frac{1}{2}\Delta z$. The constants of proportionality were then calculated on each step such that $\partial\langle\bar{u}\rangle/\partial t$ and $\partial\langle\bar{\Theta}\rangle/\partial t$ were zero. Similarly, we desire $\langle\bar{v}\rangle=0=\partial\langle\bar{v}\rangle/\partial t$ at $z=0$, whereas (17) only gives, in the mean, $\partial^2\langle\bar{v}\rangle/\partial z^2=0$ at $z=\frac{1}{2}\Delta z$. With finite differences of second-order accuracy, and with grid levels for \bar{v} (and also \bar{u} , $\bar{\Theta}$) at levels $\Delta z/2$, $3\Delta z/2$, . . . , the desired requirement is

$$(\partial\langle\bar{v}\rangle/\partial t)_{\Delta z/2} = \frac{1}{3}(\partial\langle\bar{v}\rangle/\partial t)_{3\Delta z/2}.$$

This requirement was directly enforced at each time step, and is equivalent to adding a spatially constant term to the $\partial\langle\bar{v}\rangle/\partial t$ equation at $z=\frac{1}{2}\Delta z$, as would occur if $\partial^2\langle\bar{v}\rangle/\partial z^2$ had not been assumed zero at $z=\frac{1}{2}\Delta z$.

The boundary conditions involving vertical derivatives were determined through use of grid points $\frac{1}{2}\Delta z$ to the exterior of the region treated, at which appropriate values were inserted to give second-order accuracy.

f. Finite-difference grid and formulations

The simple, space-staggered grid described by numerous authors (Harlow and Welch, 1965; Lilly, 1965; Williams, 1969) was used. Grid volumes or "cells" are defined with \bar{P}'' evaluated at the center, \bar{u} at the middle of the upstream and downstream faces, \bar{v} in the middle of the two cross-stream faces, and \bar{w} in the middle of the bottom and top faces. $\bar{\Theta}$ was evaluated at the same locations as \bar{P}'' , rather than at the location of \bar{w} , in order that boundary condition (18) could be applied at the same distance from the lower boundary as was (16). The grid volumes are placed such that \bar{w} values are centered at horizontal boundaries where $\bar{w}=0$. With the use of such a grid, the derivative in a non-linear advective term may be represented essentially by a difference across a single grid interval, rather than across two intervals as in the non-staggered mesh system. The latter system was found to give very poor results in comparison with the space-staggered mesh in a test of finite-difference methods (Orszag, 1971).

The nonlinear terms were differenced after the manner of Lilly (1965) or Harlow and Welch (1965) which conserves total kinetic energy in the absence of time differencing errors.

Eq. (6) for \bar{P}'' , with $\partial \bar{u}_i / \partial x_i$ set to zero at the new time-step level, was solved exactly with the aid of a semi-fast Fourier transform programmed by F. Lipps (unpublished). By this means, the velocity divergence at each grid point was typically maintained at 10^{-13} of the average value of $|\partial \bar{u} / \partial x|$.

The eddy coefficients K_m and K_h were evaluated at the same locations as \bar{P}'' , and were calculated from (10) and (11) such that all derivatives were taken over single grid intervals before squaring and centering them at the \bar{P}'' locations. The finite-difference formulation is given in Deardorff (1971).

Leap-frog time differencing was used, except that the diffusion terms were lagged in time (although K_m and K_h were centered in time). Once each 20 time steps the dependent variables were smoothed *in time* to avoid gradual decoupling of odd and even time-step values and subsequent instability (Williams, 1969). The time step usually employed had a dimensionless magnitude of 0.0036.

g. Discussion of truncation error

Orszag has shown that the Galerkin (or truncated Fourier-expansion) method is much more accurate than, and about equally efficient as, the physical-space finite-difference method employed here in a test of the "color" equation. In this test, a small cone-shaped area of scalar values is advected by a fixed flow of solid rotation, so that the exact solution is known at all times. There are several reasons, however, why his conclusion should be much weaker if applied to the present problem.

First, the coordinate system here is moved with the overall mean flow, thereby removing most ($\sim 85\%$) of the phase truncation errors which would otherwise be large with respect to small-scale features.

Second, our use of Reynolds averaging, along with simulation of a fluid having a $k^{-5/3}$ spectrum near the grid scale, guarantees that relatively little energy resides on those small scales for which Orszag's test applied. Actually, the spectrum of a grid-volume averaged inertial-subrange variable should exceed even -4 in slope at a scale of twice the grid interval.

Third, the presence and simulation of SGS motions in the present problem introduces non-predictable or uncertain effects which render less relevant the superiority of the Galerkin approach for the long-range prediction of fluid motion details.

Finally, the presence of buoyancy and Coriolis terms in the present problem introduces important non-differentiated terms for which truncation errors are non-existent. The mean fields $\langle \bar{u} \rangle$, $\langle \bar{v} \rangle$ and $\langle \bar{\Theta} \rangle$, when their curvature is not too large, act similarly with

respect to the vertical advection terms which are of primary importance. No such non-differentiated terms were included in the test with the color equation. Hence, the Galerkin approach, although superior to the present approach if boundary conditions (16)–(18) could be incorporated, may not be nearly as superior as a test of the color equation alone would suggest.

3. Numerical results

A dimensionless time of from 1 to 2 was usually required for the calculated velocities and eddy structure to adjust from one statistically steady state to another having a different value of $-z_i/L$. The transition was artificially speeded up by adding a constant increment to \bar{u} , \bar{v} , or $\bar{\Theta}$ at all but the lowest level, having the same sign as the volume-mean trend with time. After final application of such an increment (of magnitude 0.1–0.2), an additional period of from 0.3–0.5 was allowed for readjustment of velocity and temperature structure.

a. Mean profiles

Vertical profiles of $\langle \bar{u} \rangle$ for the four different stabilities treated are shown in Fig. 2. Each curve, in addition to being a horizontal average, is averaged over an ensemble of about 10 realizations spaced at dimensionless time intervals of about 0.2. We see that as $-z_i/L$ increases, progressively more of the momentum deficit between $z = \frac{1}{2}\Delta z$ and $z = 1$ is wiped out by convective mixing, and the upper and central region of nearly constant $\langle \bar{u} \rangle$ thickens. The value of $\langle \bar{u} \rangle$ at $\frac{1}{2}\Delta z$ has been chosen to fit the surface-layer formulation of Businger *et al.* (1971) for $R \equiv u_*/(fz_0) = 1.5 \times 10^7$ in the neutral case, and for $R \equiv z_i/z_0 = 6.8 \times 10^6$ in the unstable case. For a different value of R , say R' , the profiles would be shifted to the left or right by the amount $k^{-1} \ln(R/R')$. As will be seen later, the vertical height scale $f\hat{z}/u_*$, where \hat{z} is the dimensional height, applies only in the

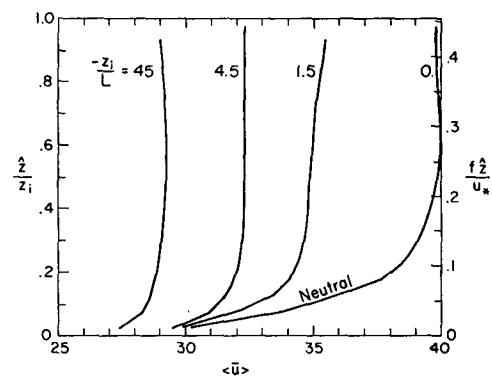


FIG. 2. Mean wind profiles (dimensionless longitudinal component) as a function of stability. Right-hand ordinate, $f\hat{z}/u_*$, applies to neutral case only; left-hand ordinate, \hat{z}/z_i , to unstable cases ($L < 0$).

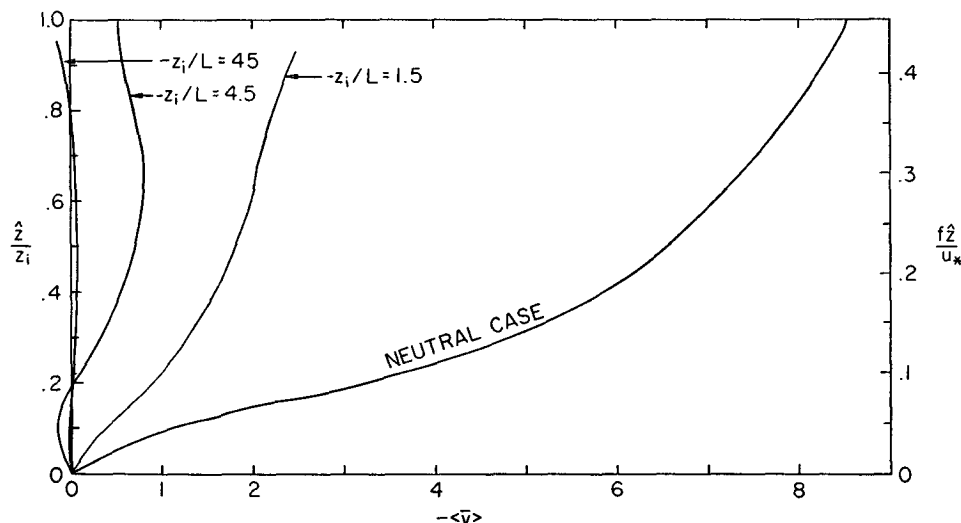


FIG. 3. Mean wind profiles (dimensionless lateral component). See Fig. 2 for description of ordinates.

neutral case. In that case, the geostrophic wind speed is approximately reached for $\hat{z} = 0.2u_*/f$.

Kuettner (1971) has related the occurrence of convective cloud streets, aligned in a downstream direction, to the occurrence of mean wind profiles having appreciable curvature in the unstable PBL. Fig. 2 indicates how such a curvature, or lack of it throughout the upper half or more of the PBL, is really a reflection of the effect of convective mixing as defined by $-z_i/L$. As will be shown later, with $-z_i/L$ as large as about 10 and more, the ordering effect caused by mean wind shear gives way to random orientation of the convective structures. Thus, little or slight curvature in $\langle \bar{u} \rangle$ above the surface layer will be shown to be indicative of randomly oriented large-scale eddy structure.

Vertical profiles of the lateral component $\langle \bar{v} \rangle$ are shown in Fig. 3. This component is diminished very drastically by only a slight degree of instability, e.g., with $-z_i/L = 1.5$. The return to geostrophic flow has to occur above the simulated inversion base at $z = 1$. The nearly unidirectional flow in the unstable PBL has been observed by Konrad (1968) and Kuettner (1971).

Vertical profiles of dimensionless potential temperature $\langle \bar{\theta} \rangle$ are shown in Fig. 4. These are similar to the profiles of $\langle \bar{u} \rangle$, except that the deficit in each case is somewhat smaller for $\langle \bar{\theta} \rangle$. This quantity has a broad maximum in the unstable cases, which corresponds to a minimum in $\langle \bar{\theta} \rangle$ since the latter is made dimensionless by the *negative* of $\langle \bar{w}\theta \rangle_s / u_*$. The minimum in $\langle \bar{\theta} \rangle$ would likely be more pronounced, due to $\partial \langle \bar{\theta} \rangle / \partial z$ being somewhat larger above the level of the minimum, if the entrainment process and the stable layer above $z = 1$ had been treated. The minimum value of $\langle \bar{\theta} \rangle$ occurred at $z = 0.68, 0.43$ and 0.34 for the respective cases of $-z_i/L = 1.5, 4.5$ and 45 . Values of $\langle \bar{\theta} \rangle$ at $z = \frac{1}{2}\Delta z$ are

again designed to be consistent with Businger *et al.* (1971), with z_i/z_0 being the same as for Fig. 2.

It should be mentioned that if one accounts for the fact that $\langle \bar{u} \rangle$ and $\langle \bar{\theta} \rangle$ are averages over Δz (as well as over the horizontal and the ensemble), the absolute values at $\frac{1}{2}\Delta z$ and above would all be shifted slightly toward smaller values, for a fixed value of h/z_0 .

b. Momentum fluxes

Dimensionless profiles of $\langle \bar{u}\bar{w} \rangle$, which include the SGS portion defined by (12) for $i = 1$ and $j = 3$, are shown in Fig. 5. The scale $f\hat{z}/u_*$ again applies only in the neutral case, while it is seen that \hat{z}/z_i is the relevant vertical scale in the unstable cases. The fact that $\langle \bar{u}\bar{w} \rangle \rightarrow 0$ then only as $z \rightarrow 1$, independent of the height u_*/f , is shown more dramatically in Fig. 6 for the unstable case with the weakest upward heat flux. The lower curve is the result of a subsequent numerical integration for the neutral case with h set to u_*/f . For the weakly

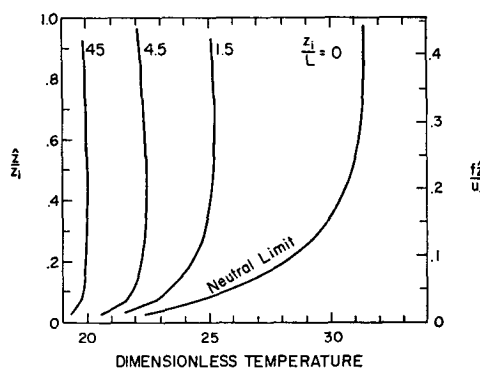


FIG. 4. Mean profiles of dimensionless potential temperature, $\langle \bar{\theta} - \theta_{vs} \rangle u_* / \langle -\bar{w}\theta \rangle_s$. See Fig. 2 for description of ordinate. The term z_i/L in the figure should be negative, not positive.

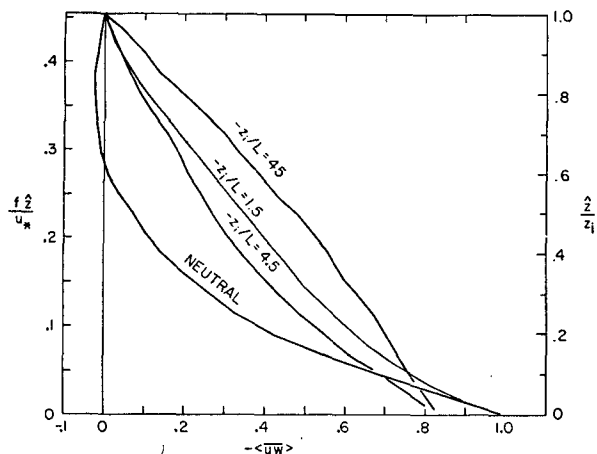


FIG. 5. Mean profiles of dimensionless momentum flux (longitudinal component). Left-hand ordinate, $f\hat{z}/u_*$, applies only to the neutral case; right-hand ordinate, \hat{z}/z_i , to unstable cases ($L < 0$).

unstable case shown, h was also set to u_*/f , yet the momentum flux easily reached up to this greater height and again vanished only as a result of the lid at z_i . Since z_i is related only accidentally (through past history), if at all, to the height $0.25u_*/f$, there is no reason to assume the height of the momentum boundary layer to be proportional to $0.25u_*/f$ in unstable cases as did Tennekes (1970) and others. Instead, the relevant height z_i should be calculated as a time-dependent quantity as has been attempted by Lilly (1968), Deardorff *et al.* (1969), and Lavoie *et al.* (1970). The rate of increase of z_i with time is usually an order of magnitude, or more, smaller than the convective velocity scale w_* to be discussed in Section 3c. Hence, z_i has here been considered as fixed for the purpose of calculating the turbulence at heights below z_i .

Tennekes (1971) has speculated as to whether the heights of the unstable thermal and momentum boundary layers are related to each other in the case when z_i is much less than $0.25u_*/f$. To treat this case rigorously would require modeling the stable layer

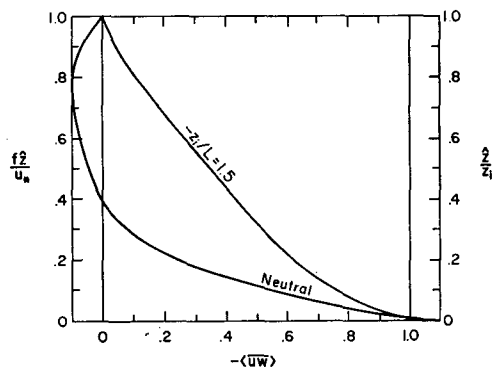


FIG. 6. Mean profiles of dimensionless momentum flux (longitudinal component) for the neutral case (left-hand ordinate) and the slightly unstable case $-z_i/L = 1.5$ (right-hand ordinate).

above z_i . However, there is little doubt that both boundary layers are again nearly identical in height and confined by z_i . A very small value of z_i is often caused by a strong subsidence inversion which easily prevents turbulent fluxes from existing up to the much greater height of $0.25u_*/f$, especially near the equator where $f \rightarrow 0$.

In the cases $-z_i/L = 1.5$ and 4.5 , Fig. 5 shows the stress profiles to be curved in the sense of a somewhat greater stress gradient near the surface than near z_i . In the case $-z_i/L = 45$ the opposite curvature occurred, but it may not be a statistically significant deviation from a linear stress profile.

In the more unstable cases, $\langle \overline{uw} \rangle$ at $z=0$ averaged nearer -0.8 than to the equilibrium value of -1 . This means that the mean wind was still gradually accelerating aloft relative to its fixed value at $z = \frac{1}{2}\Delta z$. This discrepancy occurred because of the tendency for momentum to be transported downward in occasional strong "bursts" over the entire area modeled. During a burst, $\langle -\overline{uw} \rangle$ near and above the surface ranged up to several times larger than its equilibrium surface value. These occurrences, which were triggered either by an increase of $-z_i/L$ or by addition of an increment to \bar{u} above $z = \frac{1}{2}\Delta z$, as described earlier, were considered non-representative at the time the numerical data were gathered. It is now realized that at least one of these infrequent bursts should have been included in the ensemble of realizations which were analyzed. During a burst, $\langle \bar{u} \rangle$ aloft decelerates relatively rapidly because of the greatly enhanced surface friction. The burst lasts long enough for the deceleration to cause $\langle \bar{u} \rangle$ to undershoot its equilibrium values relative to $\langle \bar{u} \rangle$ at $z = \frac{1}{2}\Delta z$. This decreased low-level shear causes $\langle -\overline{uw} \rangle$ to be less than unity. The return toward equilibrium in the profiles of $\langle \bar{u} \rangle$ and $\langle -\overline{uw} \rangle$ is quite slow, because $\partial \langle \overline{uw} \rangle / \partial z$ is then only slightly deficient in magnitude from its equilibrium value of about unity. Hence, the bursts are infrequent and short-lived, and could mistakenly be considered nonrepresentative when triggered by numerical means. No such bursts were observed in the neutral and slightly unstable cases, where $\langle -\overline{uw} \rangle$ is near unity at $z=0$. Bursts of momentum have been observed by Haugen *et al.* (1971) in unstable cases at intervals on the order of 15 min. Although the period covered in the integration without bursts is comparable to 1 hr, it is reasonable to suppose that if one were to move downstream with the mean flow within a volume of $4h \times 4h \times h$ in the unstable PBL, a momentum burst might not occur within this longer time period unless triggered by a change in surface conditions.

During a momentum burst, the heat flux was also found to be enhanced but by a smaller factor. The $\langle \Theta \rangle$ profile was able to adjust more rapidly than $\langle \bar{u} \rangle$ following such a burst, and the ensemble-averaged

heat-flux profile practically coincided with the equilibrium profile shown in Fig. 1 by the solid curve.

Vertical profiles of $\langle \bar{v}\bar{w} \rangle$ are shown in Fig. 7. They are positive (a Northern Hemisphere latitude was modeled) at all levels above the surface even though $\partial\langle \bar{v} \rangle / \partial z$ became weakly positive (see Fig. 3) at upper levels with stronger instability. The larger $-z_i/L$ becomes, the more difficult it is to obtain statistical significance in $\langle \bar{v}\bar{w} \rangle$, judging from the vertical scatter in individual values for $-z_i/L=45$. A finite positive value for $\langle \bar{v}\bar{w} \rangle$ occurred at $z=0$ in the neutral and slightly unstable cases because of the significant shear then in $\langle \bar{v} \rangle$ as $z \rightarrow 0$. Such results could be avoided, in future integrations, by specifying $\partial\langle \bar{v} \rangle / \partial z = 0$ at $z=0$, which could be implemented by adding $\partial^2\langle \bar{v} \rangle / \partial z^2 = (2/3)\langle \bar{v}(3\Delta z/2) \rangle / (\Delta z)^2$ to the right side of (17).

In the neutral case, $\langle \bar{v}\bar{w} \rangle$ is seen from Fig. 7 to approach zero nearly linearly for quite some distance below the top of the model, and this result raises the question of how far below $\hat{z}=h$ the improper influence of the lid was felt. The second integration for the neutral case previously mentioned, having $h=1.0u_*/f$, showed similar behavior but with $\langle \bar{v}\bar{w} \rangle$ first crossing zero and becoming negative at $z=0.62u_*/f$ instead of at $0.45u_*/f$. It appears, therefore, that the imposition of the lid at $0.45u_*/f$ caused the y component of the frictional force to be about 30% too intense in the upper half of the PBL.

c. Turbulence intensities

Vertical profiles of the vertical velocity intensity are shown in Fig. 8. This turbulence component is seen to be enhanced, relative to u_*^2 , with any input of thermal energy. The SGS portion which is included

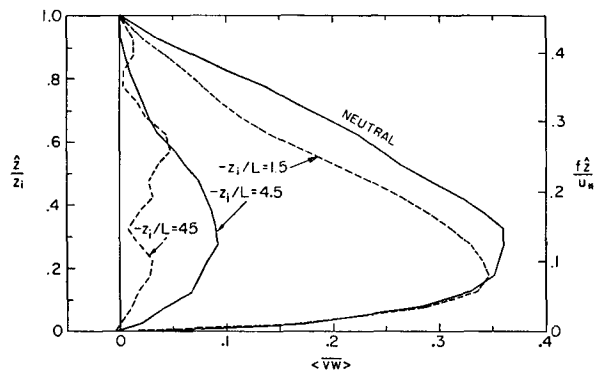


FIG. 7. Mean profiles of dimensionless momentum flux (lateral component). See Fig. 2 for description of ordinates.

was obtained from (14). At $z=0.10$ about 85% of $\langle \bar{w}^2 \rangle$ typically existed on the sub-grid scale, but this fraction dropped to about 35% for $z > 0.45$. Because of the SGS contributions, $\langle \bar{w}^2 \rangle$ does not approach zero at $z=1$.

If $\langle \bar{w}^2 \rangle$ is scaled by the convective velocity scale

$$w_* = \left(\frac{g}{\theta_{vm}} \langle \bar{w}\bar{\theta}_v \rangle_{sz_i} \right)^{\frac{1}{2}},$$

the scaled values essentially agree for the two most unstable cases at heights well above the surface layer (see right-hand dotted and solid curves with respect to the upper abscissa). The ratio u_*^2/w_*^2 in the upper abscissa of Fig. 8 is equivalent to $[-z_i/(kL)]^{-\frac{1}{3}}$, and multiplication of $\langle \bar{w}^2 \rangle$ by this ratio cancels out u_*^2 . Surprisingly, Wyngaard *et al.* (1971) found that the same scaling, with z_i being replaced by \hat{z} , holds even

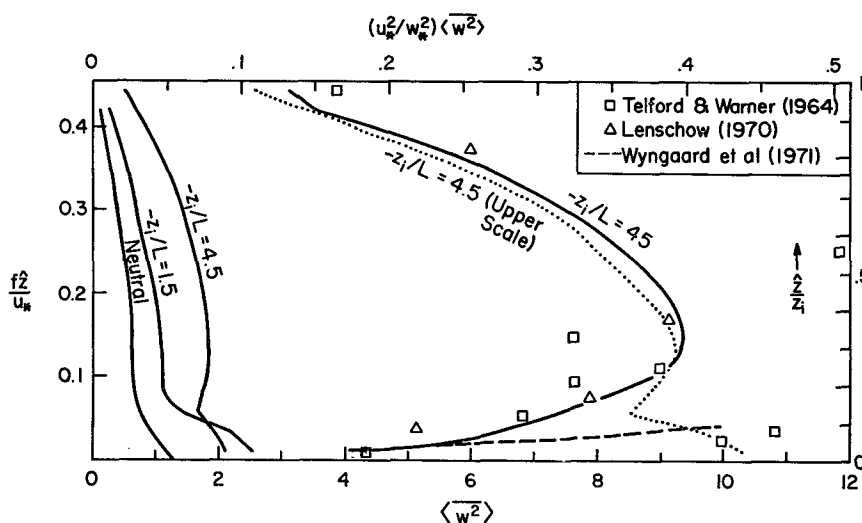


FIG. 8. Mean profiles of vertical velocity variance, made dimensionless by u_*^2 (lower abscissa) or by w_*^2 (upper abscissa). Lower abscissa applies to all solid curves; upper abscissa applies to $-z_i/L=45$, to the dotted curve, and to data points and empirical dashed curve. See Fig. 5 for a description of the ordinates.

within the surface layer in unstable conditions. They suggest that

$$\langle w^2 \rangle = (1.9)^2 \left(-\frac{\hat{z}}{L} \right)^{\frac{2}{3}} = 3.8 \left[\frac{\hat{z}}{z_i} \left(-\frac{\hat{z}}{L} \right) \right]^{\frac{2}{3}}. \quad (19)$$

The present results agree with (19) for $\hat{z}/z_i = 0.03$ at large instability (see the dashed curve of Fig. 8), but suggest that (19) should not be applied above $z = 0.05$ or 0.10 . The above relation, $\langle w^2 \rangle \propto \hat{z}^{\frac{2}{3}}$, was first deduced by Priestley (1954) for the case of strong convection and confirmed approximately by Myrup (1967) from low-level aircraft measurements above a desert during midday. However, the theory and measurements have left open the question of how high the region of validity extends relative to z_i .

Measured values shown by data points in Fig. 8 are from aircraft observations of Telford and Warner (1964) and Lenschow (1970), including two unpublished data points of Lenschow. These values, as well as the curve of Wyngaard *et al.*, refer to the upper abscissa of PBL free-convection scaling. The data points of Lenschow agree very well with the numerical results, but the earlier measurements of Telford and Warner show more scatter.

As reported previously, Fig. 8 indicates that the PBL free-convection scaling occurs most easily at upper levels in the PBL and extends to smaller heights as $-z_i/L$ increases. The figure tends to suggest that this scaling for $\langle w^2 \rangle$ commences above a height roughly equal to $-L$.

If $\langle w^2 \rangle$ is averaged throughout the PBL for the most unstable case, it is found that $\langle w^2 \rangle_m = 0.75 (-z_i/L)^{\frac{1}{2}}$. The coefficient is essentially the same as that deduced by Tennekes [1970, Eq. (13)] if his height h is set equal to z_i .

The longitudinal turbulence intensity, $\langle (\bar{u}'')^2 + \bar{u}'^2 \rangle$, which includes the resolvable and the SGS portions, respectively, is shown in Fig. 9 for the four cases.

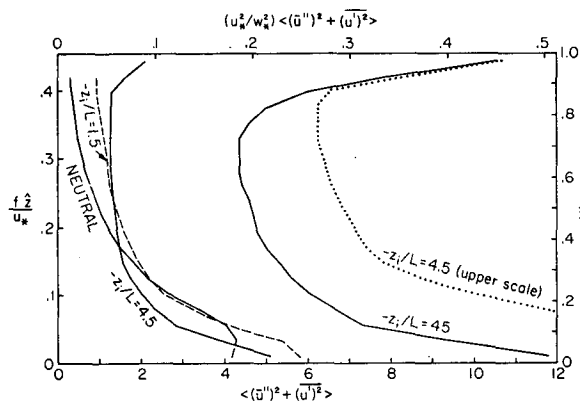


FIG. 9. Mean profiles of longitudinal velocity variance, made dimensionless by u_*^2 (lower abscissa) or by w_*^2 (upper abscissa). Lower abscissa applies to solid and dashed profiles; upper abscissa to $-z_i/L = 45$ and to dotted profile. See Fig. 5 for a description of the ordinates.

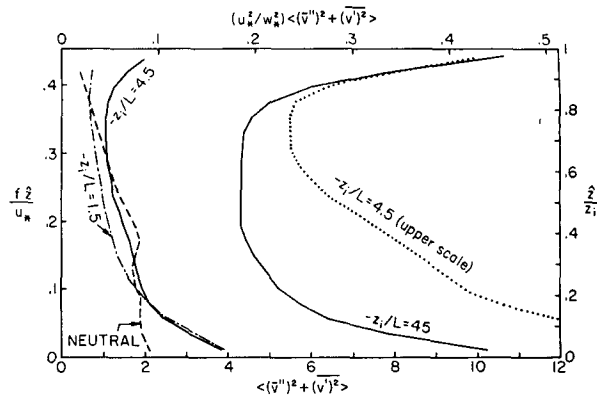


FIG. 10. Same as Fig. 9 except for lateral velocity variance.

Again the PBL free-convection scaling has been included on the upper abscissa, and profiles for the two most unstable cases may be read from this scale. For the longitudinal intensity, this scaling probably applies throughout most of the PBL in the most unstable case, but only in the upper 10% of the PBL for $-z_i/L = 4.5$. In spite of uncertainties arising from the upper boundary conditions, it appears safe to conclude that the horizontal velocity component requires a significantly greater value of $-z_i/L$ before its turbulence intensity scales with w_*^2 than does the vertical velocity component.

The strong secondary maximum at $z = 1$ in Fig. 9 is caused by outflow from impinging thermal plumes. Because of the unrealistic rigidity of the lid imposed at $z = 1$, Fig. 9 must exaggerate this secondary maximum.

At levels in the vicinity of $z = 0.1-0.2$, it is seen that the moderately unstable PBL has somewhat less longitudinal turbulence intensity (relative to u_*^2) than does the slightly unstable PBL. This result is associated with the greatly decreased mean shear in the more unstable case at low levels. For still greater instability ($-z_i/L = 45$), the transfer of kinetic energy from the vertical to the horizontal components, via the pressure forces, is able to cause enhanced longitudinal turbulence intensity.

An apparent deficiency in longitudinal turbulence intensity in the neutral case at the lowest two levels seems erroneously caused by the assumed equipartition of SGS kinetic energy. In reality, a somewhat greater fraction of the SGS energy must reside in \bar{u}'^2 than in \bar{v}'^2 or \bar{w}'^2 , especially in the neutral case, since the grid volume is not small enough to allow isotropy to be closely attained on the sub-grid scale when the mean shear is large. Except for the most unstable case, the small variations from case to case in the longitudinal turbulence intensity at the lowest level are therefore not considered significant. At $z = 0.075$, about 40% of the total longitudinal turbulence intensity existed on the sub-grid scale; this fraction dropped to about 20% for $z > 0.32$.

In Fig. 10 the lateral turbulence intensity is similarly presented. In the neutral case there is somewhat less intensity at low levels, and greater at higher levels, than in the longitudinal turbulence intensity. However, for $-z_i/L=1.5$ there is 30–50% more intensity in the x component than in the y component at all levels. The lateral and longitudinal intensities become nearly equal at all levels in the most unstable case, which again suggests that free convection is then dominating. At $z=0.075$, about 60% of the total lateral turbulence intensity existed on the sub-grid scale, but for $z>0.47$ this fraction dropped to about 25%.

d. Temperature variance

Profiles of this quantity are shown in Fig. 11, again with the usual scaling, which contains u_* , on the lower abscissa and with PBL free-convection scaling on the upper. (In this instance, it is the curve $-z_i/L=4.5$ which applies to both the lower and upper abscissa.) The profiles for $-z_i/L=4.5$ (solid curve) and 45 (dotted curve) may be compared with respect to the upper abscissa. The near agreement between the two curves suggests that this scaling applies in the PBL for $-z_i/L$ nearly as small as 4.5.

The dash-dot extension at the base of the profile for $-z_i/L=45$ is an attempt to correct for apparent underestimation of $\langle(\bar{\theta}')^2\rangle$ obtained from (15) with strong instability. At the level $z=0.025$, $r_{w\theta}$ in that case seemed spuriously large (0.89). The adjusted value in the profile at this level is based upon an extrapolated correlation of 0.69 obtained from Fig. 15.

The data points are from the previously mentioned aircraft measurements, and have been plotted only against the PBL free-convection scale. The agreement between Lenschow's values and either numerically

derived profile for the two most unstable cases is good in the lowest 40–50% of the PBL. Above this level, the actual variance increases again because of the entrainment process which was not modeled. The discrepancy between the numerical results and the observations becomes very great as $\hat{z} \rightarrow z_i$, and suggests that inclusion of this process should be the next step towards improvement of the model.

The measurements of Telford and Warner generally indicate a greater temperature variance, by about 50%, than those of Lenschow or of the numerical results. The measurements of Wyngaard *et al.* in the surface layer are also available, and their extension upward into the PBL is shown by the dashed curve which is in reference to the upper abscissa. The curve follows their formula

$$\begin{aligned} \langle(\bar{\theta}'')^2\rangle + \langle(\bar{\theta}')^2\rangle &= (0.95)^2 \left(\frac{-\hat{z}}{L} \right)^{\frac{3}{2}} \\ &= 0.90 \left[\frac{\hat{z}}{z_i} \left(\frac{-\hat{z}_i}{L} \right) \right]^{\frac{3}{2}}, \end{aligned} \quad (20)$$

which seems to hold remarkably well throughout most of the PBL, in comparison with the aircraft measurements of Telford and Warner.

e. Pressure fluctuations

In Fig. 12 the magnitude of the dimensionless pressure fluctuation, $\langle(\bar{P}'')^2\rangle^{\frac{1}{2}}$, is shown on the lower abscissa. In this case no estimate of the SGS portion has been made; it is probably quite small because of the steeper spectrum for pressure than for velocity or temperature in an inertial subrange. [Although \bar{P} contains the quantity $\overline{u_j' u_j'}/3$ as in (2), the latter quantity is to a large extent subtracted out of \bar{P}'' .] The decreased

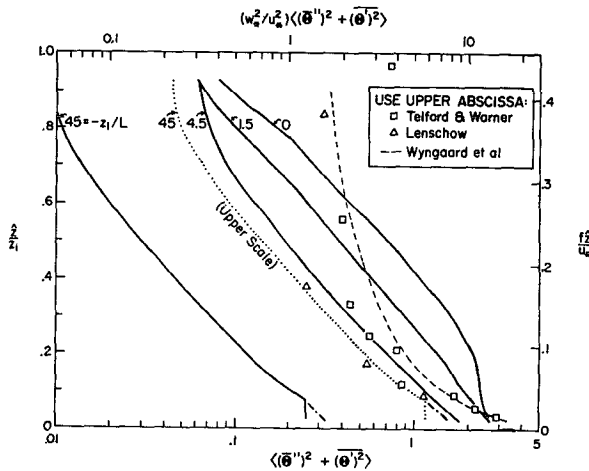


FIG. 11. Mean profiles of potential temperature variance, made dimensionless by $\langle(\hat{w}\theta')_s/u_*\rangle^2$ on lower abscissa and by $\langle(\hat{w}\theta')_s/w_*\rangle$, on upper abscissa. Lower abscissa applies to all solid profiles; upper abscissa applies to $-z_i/L=4.5$, to dotted and dashed curves, and to data points. See Fig. 2 for a description of the ordinates.

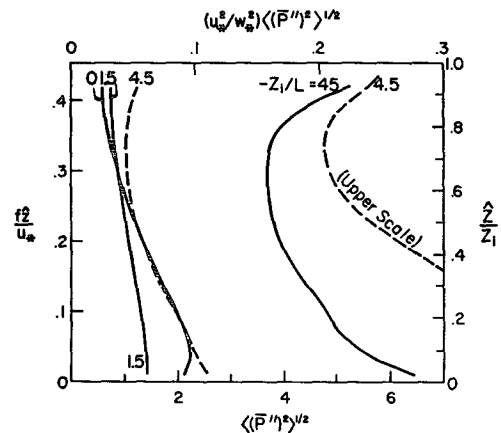


FIG. 12. Mean profiles of the pressure fluctuation, made dimensionless by ρu_* (lower abscissa) and by ρw_*^2 (upper abscissa). Lower abscissa applies to all solid profiles and to the left-hand dashed profile; upper abscissa applies to $-z_i/L=45$ and to the right-hand dashed profile. See Fig. 5 for a description of the ordinates.

magnitude of the pressure fluctuation in the lower half of the PBL for $-z_i/L=1.5$, relative to the neutral case, is somewhat surprising. It appears associated with greater elongation of the w eddies and decreased low-level mean shear in the slightly unstable case, to be described later. The shape of the pressure-fluctuation profile is similar to that of the total turbulence kinetic energy, with average magnitude 0.6 of that energy.

The two right-hand curves of Fig. 12 can be referred to the PBL free-convection scale on the upper abscissa. The disparity indicates that such scaling does not apply for $-z_i/L$ as small as 4.5.

f. Correlation coefficients

The correlation coefficient

$$r_{uw} = \langle \overline{uw} \rangle / (\sigma_u \sigma_w),$$

where σ is the standard deviation at a given level and includes the SGS contribution, is shown in Fig. 13. A large increase in $-r_{uw}$ aloft is seen to occur in passing from the neutral case (for which the ordinate \hat{z}/u_* applies) to the unstable case $-z_i/L=1.5$ (for which the ordinate \hat{z}/z_i applies). This result thus only reflects the fact that the momentum flux is mostly confined below $0.3u_*/f$ in the neutral case. As $-z_i/L$ is increased further, $-r_{uw}$ is seen to decrease substantially. This result becomes clear when it is realized that dimensionless values of $\langle -\overline{uw} \rangle$ remain bounded between 1 and 0 while the dimensionless turbulence intensity product $\sigma_u \sigma_w$ (in the denominator) increases with increasing thermal instability. The product $\sigma_u \sigma_w$ was composed mainly of SGS motions below $z=0.3$, and mainly of resolvable motions above this level.

Apparently, the transport of momentum in bursts in the more unstable cases and the small values of $-r_{uw}$ which then occur are responsible for the greater difficulty in measuring reliable values of $\langle \overline{uw} \rangle$ from aircraft (Lenschow, private communication) than of sensible heat flux. The coefficient $r_{w\theta}$ will be seen to be considerably larger than $-r_{uw}$.

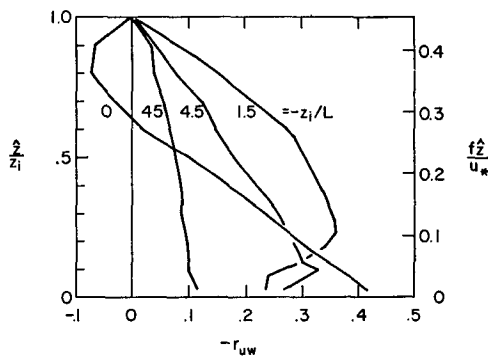


FIG. 13. Mean profiles of the correlation coefficient $-r_{uw}$ as a function of stability. Ordinates are as described in the legend of Fig. 2.

The profile of $-r_{uw}$ in neutral conditions is practically identical to that shown in D1 but is somewhat smoother because of the greater horizontal area modeled here ($4h \times 2h$ as opposed to $3h \times h$ in D1). However, failure of $-r_{uw}$ to approach a value of ~ 0.4 as $z \rightarrow 0$ in the case of $-z_i/L=1.5$ appears erroneous and could be caused by inaccuracy in assumption (14) for the SGS variances.

The correlation coefficient, $r_{vw} = \langle \overline{vw} \rangle / (\sigma_v \sigma_w)$, is shown in Fig. 14. It decreases with increasing instability even more rapidly than does $\langle \overline{vw} \rangle$. The strong resemblance in the shape of the neutral profile to that of the slightly unstable profile occurs only because h was chosen to be $0.45u_*/f$ in the neutral case.

The correlation coefficient, $r_{w\theta} = \langle \overline{w\theta} \rangle / (\sigma_w \sigma_\theta)$, is shown in Fig. 15. For the neutral case, the values are limiting in the sense that both $\langle \overline{w\theta} \rangle$ and σ_θ are vanishingly small, and the passive temperature fluctuations do not then affect the vertical velocity. In that case, $r_{w\theta}$ could be of either sign, depending upon the sign of the negligibly small surface heat flux. An unrealistic feature of this case is that the height of the passive-scalar boundary layer was forced to be h by (9), whereas its actual height in the neutral limit should be determined by the shear-generated turbulence to be some particular fraction of u_*/f . However, with $h=0.45u_*/f$ the discrepancy is not serious at low levels, and inclusion of the limiting case allows us to see from Fig. 15 that the correlation is quite high even in the absence of any buoyancy effect; i.e., $\bar{\theta}$ depends upon \bar{w} although \bar{w} does not depend upon $\bar{\theta}$. With slight instability and with \bar{w} then becoming partially dependent upon $\bar{\theta}$, it is surprising that $r_{w\theta}$ decreases at lower levels. For $\hat{z} < 0.6z_i$, $r_{w\theta}$ is seen to increase systematically with increased thermal instability in the unstable cases.

The correlation coefficient, $r(\bar{u}'', \bar{\theta}'') = \langle \bar{u}'' \bar{\theta}'' \rangle / (\sigma_{\bar{u}''} \sigma_{\bar{\theta}''})$, is shown in Fig. 16. No good estimate of the SGS contribution to the correlation was available, and

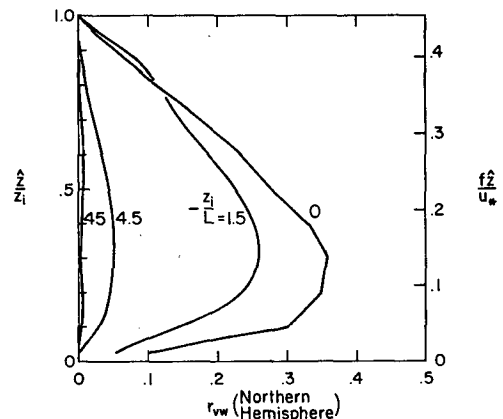


FIG. 14. Mean profiles of the correlation coefficient r_{vw} (positive in the Northern Hemisphere). Ordinates are as described in legend of Fig. 2.

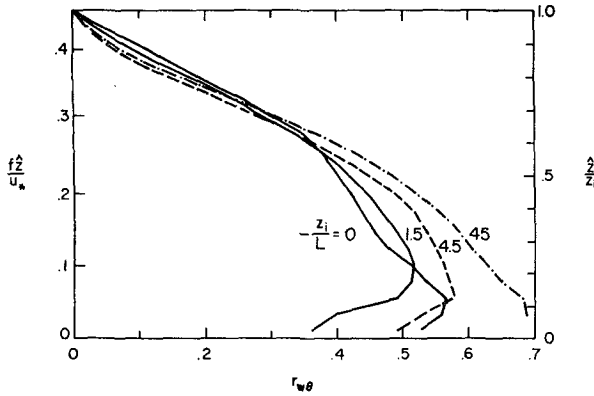


FIG. 15. Mean profiles of the correlation coefficient $r_{w\theta}$ (positive with upward heat flux). Ordinates are as described in legend of Fig. 5.

only the directly calculated values were used in this instance. The correlation is of the same sign as observed in the lower atmosphere, upon remembering that $\bar{\Theta}$ is made dimensionless by the negative of the surface heat flux. The correlation in the limiting neutral and slightly unstable cases is quite high, in the vicinity of 0.8, for the reason explained by Webb (1970). His explanation concerns the similarity between the equations for $\partial \bar{u}''/\partial t$ and $\partial \bar{\Theta}''/\partial t$ near the surface where the dimensionless vertical advection terms are similar and relatively large. Thus, every fluctuation of vertical velocity tends to drive \bar{u}'' and $\bar{\Theta}''$ towards equality, with the fluctuating pressure gradient in the $\partial \bar{u}''/\partial t$ equation being the main source of dissimilarity. The failure of the neutral case to show slightly greater correlation near the surface than for $-z_i/L=1.5$ is believed to be a result of excessive irregularity in the $\bar{\Theta}$ field on a small scale, associated with use of $K_h/K_m=2$ in the neutral case instead of the value 3 which was later realized to be preferable. Values of this correlation coefficient in excess of 0.9 have been observed by Webb during stable stratification within the surface layer.

With increased instability or height we see from Fig. 16 that the correlation drops, the reason being that

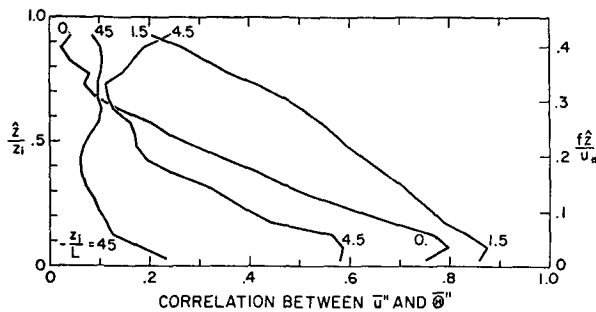


FIG. 16. Mean profiles of the correlation coefficients $r(\bar{u}'', \bar{\Theta}'')$ (positive with upward heat flux). Ordinates are as described in legend of Fig. 2.

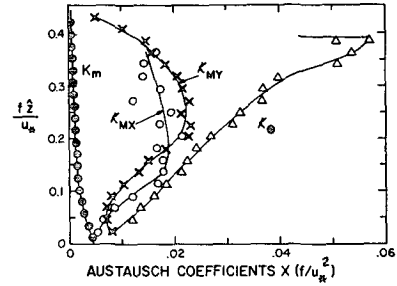


FIG. 17. Mean (neutral case) profiles of large-scale eddy coefficients or Austausch coefficients for momentum (\mathcal{K}_{mx} and \mathcal{K}_{my}) and for heat (\mathcal{K}_θ), and mean profile of sub-grid-scale eddy coefficient \mathcal{K}_m , made dimensionless by u_*^2/f .

$\partial \langle \bar{u} \rangle / \partial z$ and $\partial \langle \bar{\Theta} \rangle / \partial z$ then become much smaller and the dissimilarity between the two equations becomes greater. Lenschow (private communication) has measured the value 0.37 for the total correlation at $z=0.1$ when $-z_i/L$ was probably of order 10. The value from the figure for this degree of instability is about 0.4 or 0.5, and is expected to be slightly high because of omission of all SGS contributions in $r(\bar{u}'', \bar{\Theta}'')$.

g. Large-scale eddy coefficients

Using the present notation, the usual large-scale eddy coefficients are defined by

$$\mathcal{K}_{mx} = -\langle \bar{u}\bar{w} \rangle / (\partial \langle \bar{u} \rangle / \partial z),$$

$$\mathcal{K}_{my} = -\langle \bar{v}\bar{w} \rangle / (\partial \langle \bar{v} \rangle / \partial z)$$

$$\mathcal{K}_\theta = -\langle \bar{w}\bar{\theta} \rangle / (\partial \langle \bar{\theta} \rangle / \partial z),$$

where \mathcal{K} in the neutral case is with respect to the passive scalar. Only the neutral case will be considered here because in unstable cases the \mathcal{K} 's generally pass through $\pm \infty$ and become negative aloft in the PBL. The results for the neutral case are shown in Fig. 17 in which the SGS eddy coefficient for momentum is also shown. Because this SGS coefficient is so much smaller than either \mathcal{K}_{mx} or \mathcal{K}_{my} above the lowest one or two grid levels, there is reason to believe that assumptions (10) and (11) were not at all crucial in the derivation of the mean profiles shown in Figs. 2-4.

In Fig. 17 we see that \mathcal{K}_{mx} and \mathcal{K}_{my} reach maxima of about $0.02u_*^2/f$, with the former reaching this maximum at a height near $0.18u_*/f$ and the latter at a higher level of about $0.25u_*/f$. The eddy coefficient for heat, \mathcal{K}_θ , is generally 30-50% larger than the eddy coefficients for momentum. This result is consistent with the finding in the surface layer (Businger *et al.*) that $\mathcal{K}_\theta/\mathcal{K}_{mx} \approx 1.3$ in near-neutral conditions.

h. Turbulence energy budget

This budget in the neutral case turned out very similar to that presented in D1 and will not be described here.

In unstable cases, the rate of production of turbulence kinetic energy by mean wind shear became less than 10% of the rate of production by buoyancy above a height of $0.38z_i$ for $-z_i/L=4.5$ and $0.07z_i$ for $-z_i/L=45$. (It was nowhere unimportant in the case $-z_i/L=1.5$). As in the energy budget measured by Lenschow (1970), the divergence of $\langle \bar{w}\bar{u}_j''\bar{u}_j''/2 \rangle$ was positive at lower levels and negative aloft, with the cross-over occurring at a level between 0.3 and $0.4z_i$. As emphasized by Zubkovskiy and Koprov (1970), this term was found to be quite important at higher levels, and exceeded the rate of production due to buoyancy above a height of 0.5 to $0.6z_i$. The divergence of $\langle \bar{w}\bar{P}'' \rangle$ tended to have the opposite sign from that of the kinetic energy transport, and a magnitude of about 0.2 – 0.4 of the latter.

The temperature-variance budget was examined for $-z_i/L=45$, and because of slightly countergradient values of $\partial\langle\bar{\Theta}\rangle/\partial z$ aloft, the production term, $-\langle\bar{w}\bar{\Theta}\rangle$ ($\partial\langle\bar{\Theta}\rangle/\partial z$), became negative above $0.36z_i$. Above $0.5z_i$ this term remained nearly equal in magnitude to the

rate of removal of $\frac{1}{2}\langle\bar{\Theta}''^2\rangle$ by transfer to subgrid scales. The level above which more variance is gained from below than is exported aloft was only $0.16z_i$.

4. Turbulence structure

The main question in the minds of many investigators of the PBL is the degree of prominence of Ekman-like vortices, elongated in a downstream direction, and the conditions under which they preferentially occur.

a. Synoptic views

The neutral case, though it rarely if ever occurs throughout the PBL, is of special interest because complications due to buoyancy are absent and theories are simpler. A plan view of the neutral structure in a horizontal plane at a particular time long after the initial conditions have been "forgotten" is shown in Fig. 18 for $\hat{z}=0.05h=0.023u_*/f$. A similar view for $\hat{z}=0.25h=0.11u_*/f$ at the same time is shown in Fig. 19. In the lower level, the \bar{u} eddies are organized into

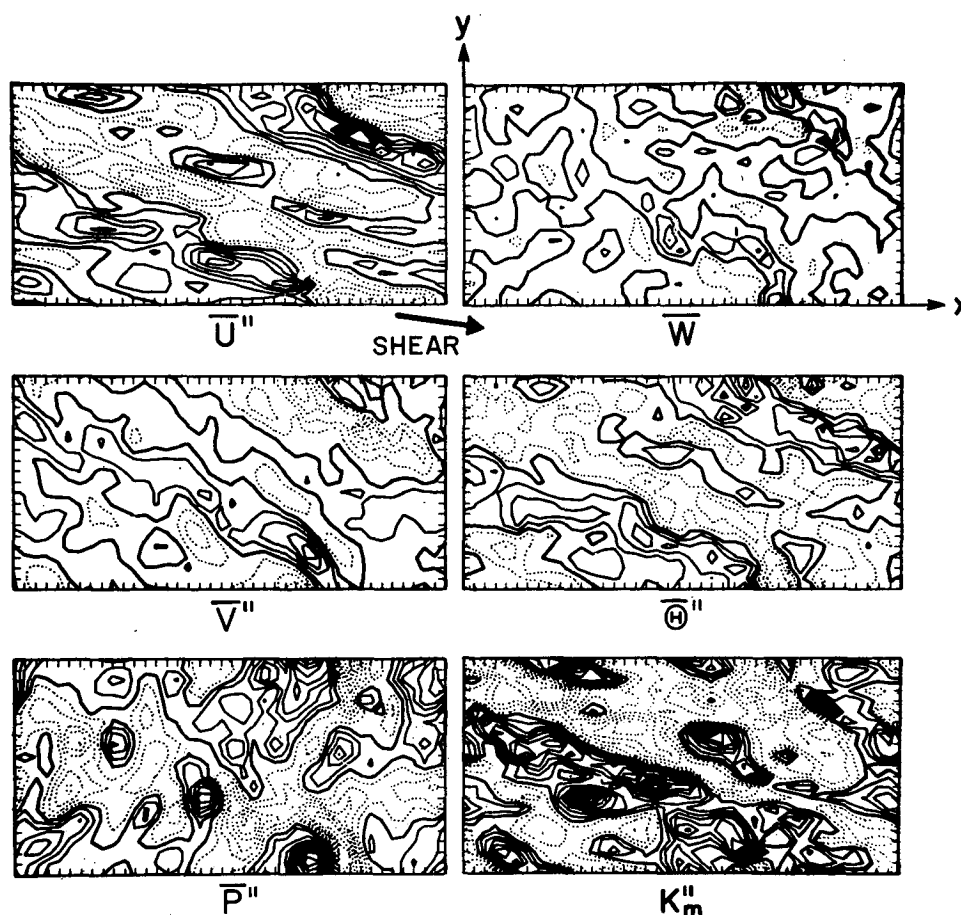


FIG. 18. Contours of \bar{u}'' , \bar{w} , \bar{v}'' , $\bar{\Theta}''$, \bar{P}'' and K_m'' in the x - y plane at $z=0.05$ at time $t=11.125$ in the neutral case. Contour intervals are 0.75 for \bar{u}'' and \bar{v}'' , 0.50 for \bar{w} , 0.75 for $\bar{\Theta}''$, 1.0 for \bar{P}'' , and 0.0005 for K_m'' . Solid contours represent values greater than the mean at that height, dotted contours less than the mean. Grid intervals along perimeter are indicated by tick marks.

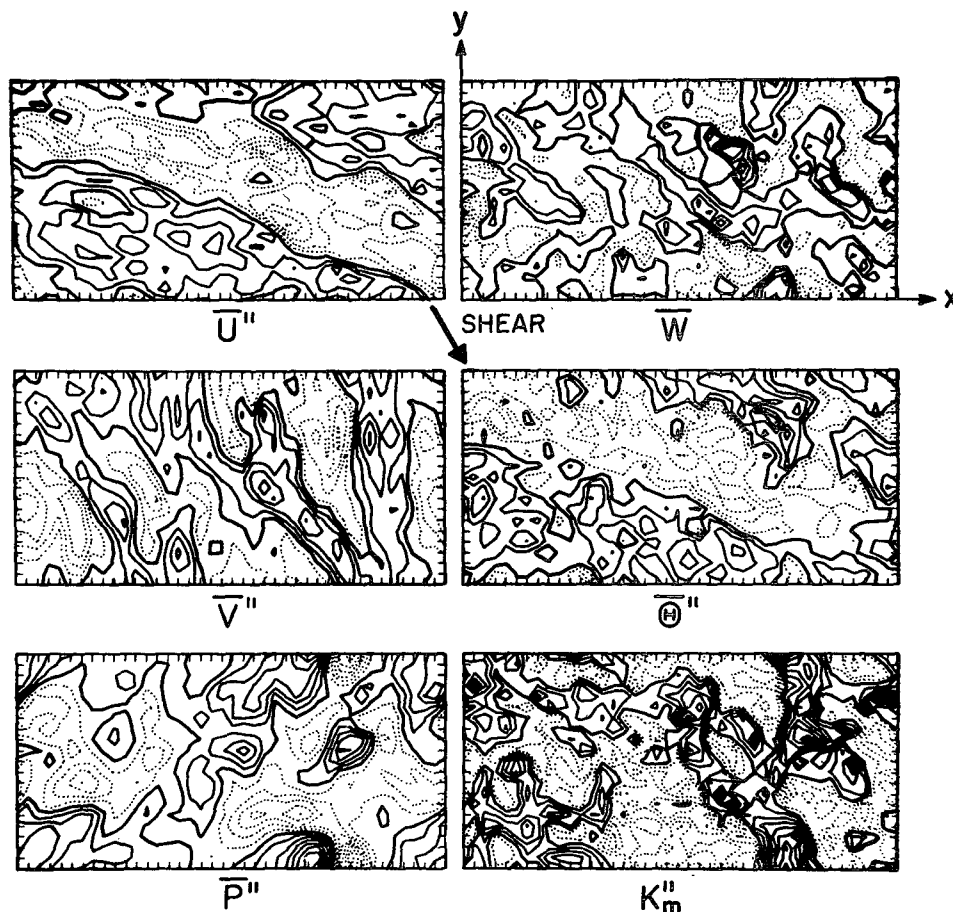


FIG. 19. Contours of \bar{u}'' , \bar{w} , \bar{v}'' , $\bar{\theta}''$, \bar{P}'' and K_m'' in the x - y plane at $z=0.25$ at time $t=11.125$ in the neutral case. Other details are described in the legend to Fig. 18.

distinct "bands" or "streaks" oriented about 15° to the right (facing downstream in the Northern Hemisphere) of the surface wind. This is found to be the angle of the mean shear vector existing at a height of about $0.04u_*/f$. (The arrow labeled "shear" in Fig. 18 gives the direction of the mean shear vector at the particular height examined.) There would be no point in comparing the orientation of the bands with the wind direction, because the latter depends upon $u_*/(fz_0)$ whereas the orientation of the bands and of the shear vector is independent of surface roughness above a homogeneous surface. The length of a band is typically three to six times (or sometimes much more) than its width, and the width is typically 0.2 to $0.6u_*/f$. (A lateral wavelength would be twice the width).

The \bar{v} eddies are more irregular but usually elongated also. Amazingly, however, their angle of alignment is usually greater, being about 25° in Fig. 18. It is still greater at the higher level where it varies from 40° to 90° .

However, the \bar{w} eddies are not similarly or distinctly elongated at either level. In the neutral case the turbulent motions are sufficiently intense to mask any such organization in \bar{w} . The results suggest, however,

that if some time averaging were performed over a limited region with respect to a coordinate system moving with the velocity of a well-defined band, the \bar{w} structures would be similarly elongated. Thus, the question of whether the structure would resemble Faller and Kaylor's (1966) type 1 instability or Lilly's (1966) type 2 instability is perhaps not meaningful. In one respect they resemble type 1 more closely, because in this type Lilly showed that the Coriolis terms are not important except in determining the mean laminar flow profile, and in the previous (D1) and present study the Coriolis terms indeed prove insignificant in transferring energy from the longitudinal to the lateral velocity component. The same holds true if the coordinate system is rotated to line up the x axis with the \bar{u} bands, with the Coriolis term, $(fh/u_*)\langle\bar{u}''\bar{v}''\rangle$, being recalculated with respect to the new coordinate axes. Since type 2 instability requires this term to dominate the energetics of the lateral velocity component, it appears that the numerical results do not resemble type 2 instability.

On the other hand, the pressure-gradient transfer term, $\langle\bar{u}''\partial\bar{P}''/\partial x\rangle$, which is assumed zero in both types of Ekman instability when the x axis is the direction

of band alignment, turns out to be the primary mechanism transferring energy from the \bar{u}'' component to \bar{v}'' and \bar{w} at low levels. In Figs. 18 and 19 it is seen that the \bar{P} eddies have no tendency to be elongated into bands, and the individual "cells" within the \bar{u} bands permit $\langle \bar{u}'' \partial \bar{P}'' / \partial x \rangle$ to be finite and positive. Hence, the banded \bar{u} structure in the turbulent PBL probably should not be considered analogous to any laminar Ekman instability for which two-dimensionality is assumed. Instead, the results more closely resemble channel-flow turbulence at large Reynolds numbers (Deardorff, 1970d) except for the absence then of rotational effects. Other difficulties in comparing with Ekman instability theory are: 1) the length scale u_* / f must be compared with $(2\mathcal{K}_{mx}/f)^{1/2}$, and the height of evaluation of \mathcal{K}_{mx} is uncertain; and 2) to be independent of surface roughness, the angle of the bands must be reckoned with respect to the angle of the surface wind and not the geostrophic flow angle as in the laminar Ekman theories.

The reason for the banded structure in \bar{u} seems due to the effect of the mean wind shear in stretching out the \bar{u} eddies. Observations of their patterns over the duration of the integration reveals that their typical lifetimes are at least 0.2 to 0.3/f, which is ample time for the mean shear to stretch a compact eddy into a length of 10 to 20 multiples of its initial height. Even though the \bar{w} eddies are not similarly elongated, instantaneously, their negative correlation with \bar{u} ensures that the \bar{u} bands tend to receive energy preferentially from $-\bar{w} \partial \langle \bar{u} \rangle / \partial z$ at various locations along the bands such as to maintain the bands.

The reason for the \bar{w} eddies in the neutral PBL not being similarly elongated is evidently the previously mentioned compensation to the effect of mean shear provided by the fluctuating vertical pressure gradient. The original term responsible for this compensation is $-2(\partial \bar{w} / \partial x)(\partial \langle \bar{u} \rangle / \partial z)$ in the right-hand side of Eq. (6) for $\nabla^2 \bar{P}''$. That this term is dominant at low levels may be seen from careful inspection of Fig. 18; \bar{P}'' tends to have the sign of $(\partial / \partial x)(\partial \langle \bar{u} \rangle / \partial z)$ in regions where this term has a large magnitude. It can be reasoned, either with the aid of figures of \bar{P}'' or with a linearized theory for constant shear, that this effect is of the proper magnitude and sign to counteract the downstream tilting effect of differential advection of \bar{w} .

The elongation of the $\bar{\Theta}''$ eddies is also attributable to the mean shear, or alternatively, to the high correlation between \bar{u}'' and $\bar{\Theta}''$ which shows up clearly in Figs. 18 and 19.

With slight instability ($-z_i/L=1.5$), the shapes of the \bar{w} eddies are elongated more like those of \bar{u} . Fig. 20 shows this for the x - y plane at $z=0.25$. The elongated \bar{w} eddies, though still more irregular in appearance than the \bar{u} eddies, are seen to be situated out of phase with the \bar{u}'' eddies such as to give the necessary negative correlation between \bar{w} and \bar{u}'' . At this slight degree

of thermal instability, the \bar{u}'' alignment has about the same angle with respect to the x axis as in the neutral case, apparently because $\partial \langle \bar{u} \rangle / \partial z$ has been decreased at low levels by convective mixing as much as has $|\partial \langle \bar{v} \rangle / \partial z|$ (see Figs. 2 and 3). The alignment of the \bar{u} and \bar{w} eddies was found to persist in this case to a height of at least $0.7z_i$. The wavelength spacing between "rolls" or "streets" ranges from 1.5 to $2.0z_i$, in agreement with the clear-air radar measurements of Konrad (1968), and up to a factor of 2 smaller than the corresponding values for cloud streets estimated by Kuettner (1971). The structure in all cases was examined in the x - y planes at $z=0.05, 0.25, 0.45, 0.65$ and 0.85 . Dominant wavelengths appeared nearly constant for $z \geq 0.25$, but often tended to be smaller at $z=0.05$ because of additional, smaller scale structures existing at this level.

The \bar{u}'' and $\bar{\Theta}''$ fields are again seen, in Fig. 20, to be well correlated because $\partial \langle \bar{u} \rangle / \partial z$ and $\partial \langle \bar{\Theta} \rangle / \partial z$ are still relatively large at low levels. The simultaneous correlation occurring between \bar{w} and $-\bar{\Theta}''$, when the latter creates buoyant motions, causes the $-\bar{w}$ field at low levels to be more similar to the $\bar{\Theta}''$ field and therefore more similar to the \bar{u}'' field. *This appears to be the reason why the flow structure bears more resemblance to Ekman vortices in the slightly unstable case than in the neutral case.*

The \bar{v} eddies of Fig. 20 are again typically aligned at larger angles away from the downstream direction than are the \bar{u} eddies, becoming more so at greater heights. A qualitative explanation is that the \bar{v} eddies tend to be aligned, at all levels, in the direction of the mean shear existing near the average height, z_v , which is strongly influenced by the rate of production of $\langle (\bar{v}'')^2 \rangle$. A reasonable definition of this height is

$$z_v = \int_0^1 z \langle -\bar{w}\bar{v} \rangle \frac{\partial \langle \bar{v} \rangle}{\partial z} dz \bigg/ \int_0^1 \langle -\bar{w}\bar{v} \rangle \frac{\partial \langle \bar{v} \rangle}{\partial z} dz.$$

This level turns out to be about $0.28z_i$ in the weakly unstable case and $0.15u_* / f$ in the neutral case. By the same reasoning, \bar{u} eddies are expected to be aligned in the direction of the mean shear near the similarly defined level of z_u . That level is about $0.16z_i$ in the weakly unstable case and $0.05u_* / f$ in the neutral case. This or similar reasoning appears necessary to explain the differing angles of alignment of the \bar{u} and \bar{v} eddies.

With an increase of $-z_i/L$ to 4.5, the structure of \bar{u}'' , \bar{w} and $\bar{\Theta}''$ is less definitely oriented in a downstream direction. However, the eddy elongation which does occur is very nearly along the direction of the surface wind, as shown in Fig. 21 for $z=0.25$. With this degree of instability, the $\bar{\Theta}$ field is seen to be better correlated with $-\bar{w}$ than with \bar{u}'' .

With $-z_i/L$ increased to 45, the orientation of the \bar{w} and $\bar{\Theta}$ eddies seems truly random as in Fig. 22. The \bar{u} eddies are seen to retain a little elongation in x , and the \bar{v} eddies in y , due to the tendency towards isotropy

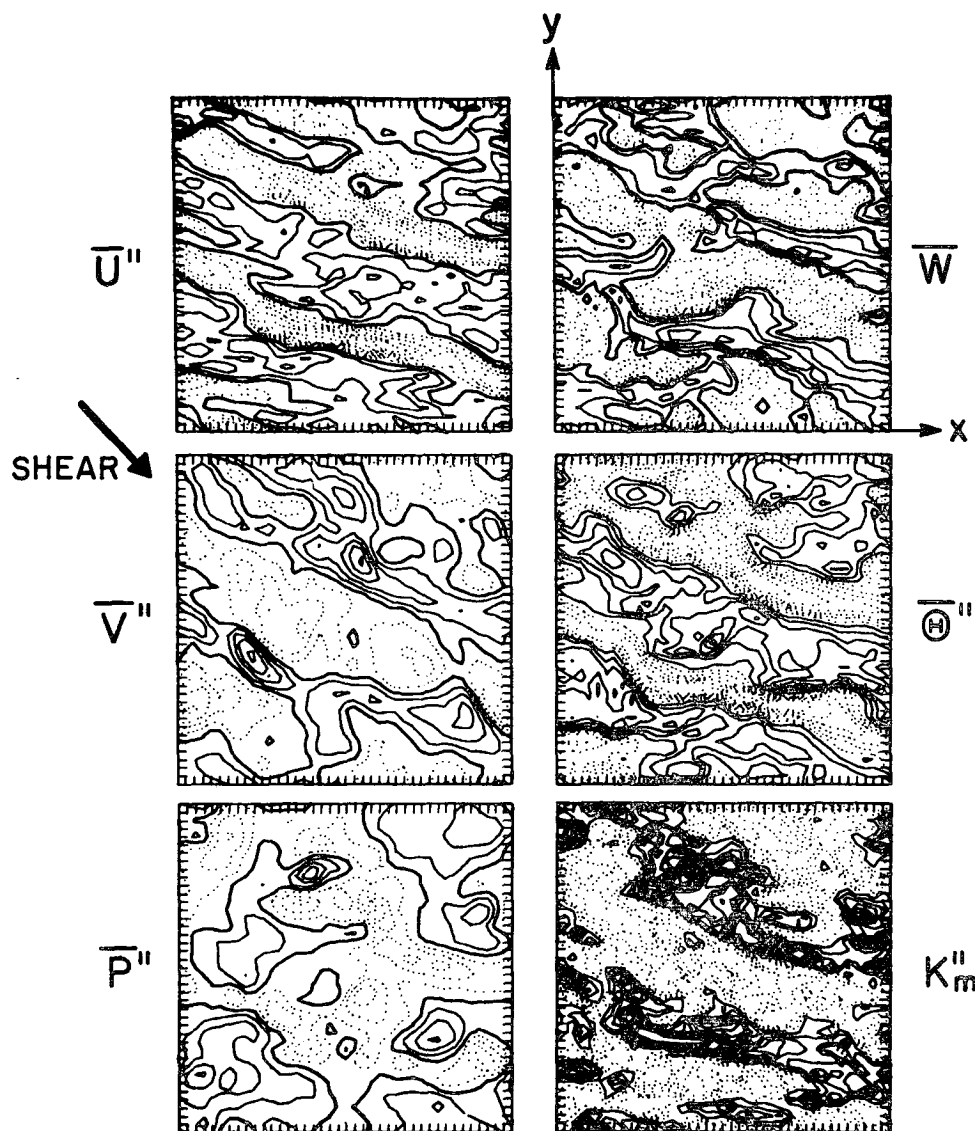


FIG. 20. Contours of \bar{u}'' , \bar{w} , \bar{v}'' , $\bar{\theta}''$, \bar{p}'' and K_m'' in the x - y plane at $z=0.25$ at time $t=2.832$ for $-z_i/L=1.5$. Contour intervals are 0.40 for $\bar{\theta}''$ and 0.0008 for K_m'' . Other details are as described in the legend to Fig. 18.

at the larger wavenumbers. The horizontal spectra for this case at $z=0.45$, presented in Deardorff (1971), showed isotropy in the horizontal: the spectrum of \bar{u}'' along y and \bar{v}'' along x were identical, as were \bar{u}'' along x and \bar{v}'' along y , \bar{w} along x and \bar{w} along y , and $\bar{\theta}''$ along x and $\bar{\theta}''$ along y . However, at this height the energy in \bar{w} along x or y exceeded that in \bar{u}'' along y by a factor of 1.8 at larger wavenumbers, and exceeded $\frac{4}{3}$ of that of \bar{u}'' along x by a factor of 2.6. Atmospheric measurements (Weiler and Burling, 1967; Smith *et al.*, 1970; Lenschow, 1970) which show the same type of behavior are becoming more plentiful—significant departures from local three-dimensional isotropy occur at frequencies well within the $-\frac{5}{3}$ subranges. The depart-

ture is always in the direction which favors the velocity component receiving most of its energy directly rather than from the pressure gradients.

These results on the structure confirm the qualitative observations of Kuettner and Konrad on the occurrence or non-occurrence of downstream alignment of \bar{w} and $\bar{\theta}$. In particular, such structures probably occur for $-z_i/L$ even closer to neutral than the value 1.5, and probably extend to $-z_i/L$ of about 10. If the tetraon observations of Angell *et al.* (1968) and Angell (1971) are accepted as evidence of alignment of the \bar{w} eddies, then the present results suggest that during those observations $-z_i/L$ was in the vicinity of 10 or less. Since the present study is restricted to equilibrium

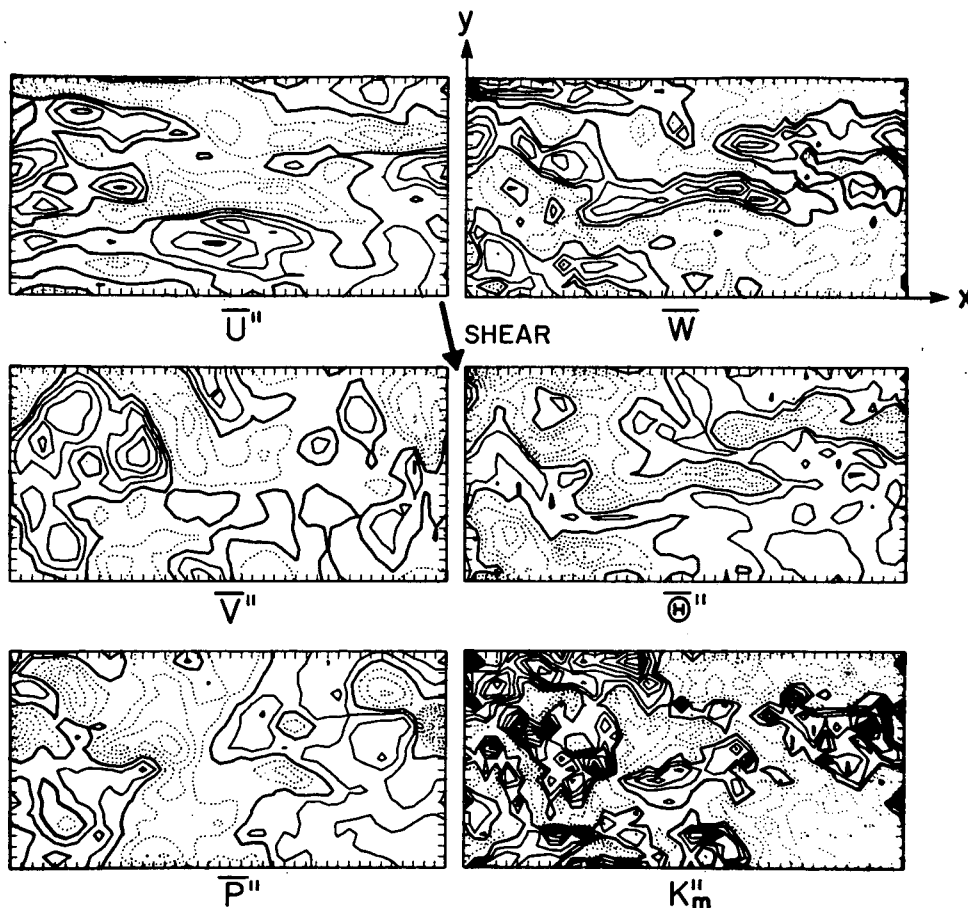


FIG. 21. Contours of \bar{u}'' , \bar{w} , \bar{v}'' , $\bar{\theta}''$, \bar{p}'' and K_m'' in the x - y plane at $z=0.25$ at time $t=9.875$ for $-z_i/L=4.5$. Contour intervals are 0.75 for \bar{w} , 0.38 for $\bar{\theta}''$, and 0.0010 for K_m'' . Other details are as described in the legend to Fig. 18.

conditions, the above results do not rule out the possibility that if $-z_i/L$ is increasing with time, elongated structures would persist after $-z_i/L$ exceeds about 10 (until the mean wind at low levels has had time to accelerate to nearly the speed existing aloft in the PBL). Also, the present results can say nothing about the possible occurrence of shear-oriented structures associated with a strong thermal wind, or with strong shear which could exist at the top of the mixed region above the level which was modeled.

Typical side views of the structure, in an x - z plane located at $y=5\Delta y$, are shown in Figs. 23–27 in order of increasing thermal instability. Figs. 23, 25, 26, 27 are for the same times as Figs. 19, 20, 21, 22, respectively. The effect of shear in $\langle \bar{u} \rangle$ in tilting the \bar{v} and $\bar{\theta}$ eddies is apparent to considerable heights in the neutral cases (Figs. 23, 24). An “eddy tilt” of \bar{u} in the x - z plane, for example, is here defined to be the inclination from the vertical of the locus of neighboring points having local maxima in curvature of the isotachs of \bar{u}'' . Such lines are easier to depict than to define, and the \bar{u}'' eddies are seen to tilt typically by about 80°

in Figs. 23 and 24. This result was also obtained in D1, and shows up more characteristically in Fig. 24 than in Fig. 23. The \bar{v} eddies are seen to have tilts which decrease with height but average only about 60°. These results appear to conflict with the observations of Pielke and Panofsky (1970) that the u eddies have “slopes” from the vertical of only about half those of the v eddies. Their method was that of examining phase differences of a selected wave component at two different heights on a tower, using Taylor’s hypothesis to convert a time difference to a spatial increment in x . Unfortunately, this method fails to describe the orientation when the major eddy axis is nearly horizontal and when the eddy height encompasses both levels of measurement. For example, if this method were applied to a hypothetical field of laminar Ekman rolls drifting past a tower, a tilt of 0° would be obtained instead of 90°. Because the calculated \bar{u} eddies are highly elongated in the x direction and typically have a thickness $\geq 20\%$ of the PBL depth, the method of Pielke and Panofsky can lead to misinterpretation of eddy shapes.

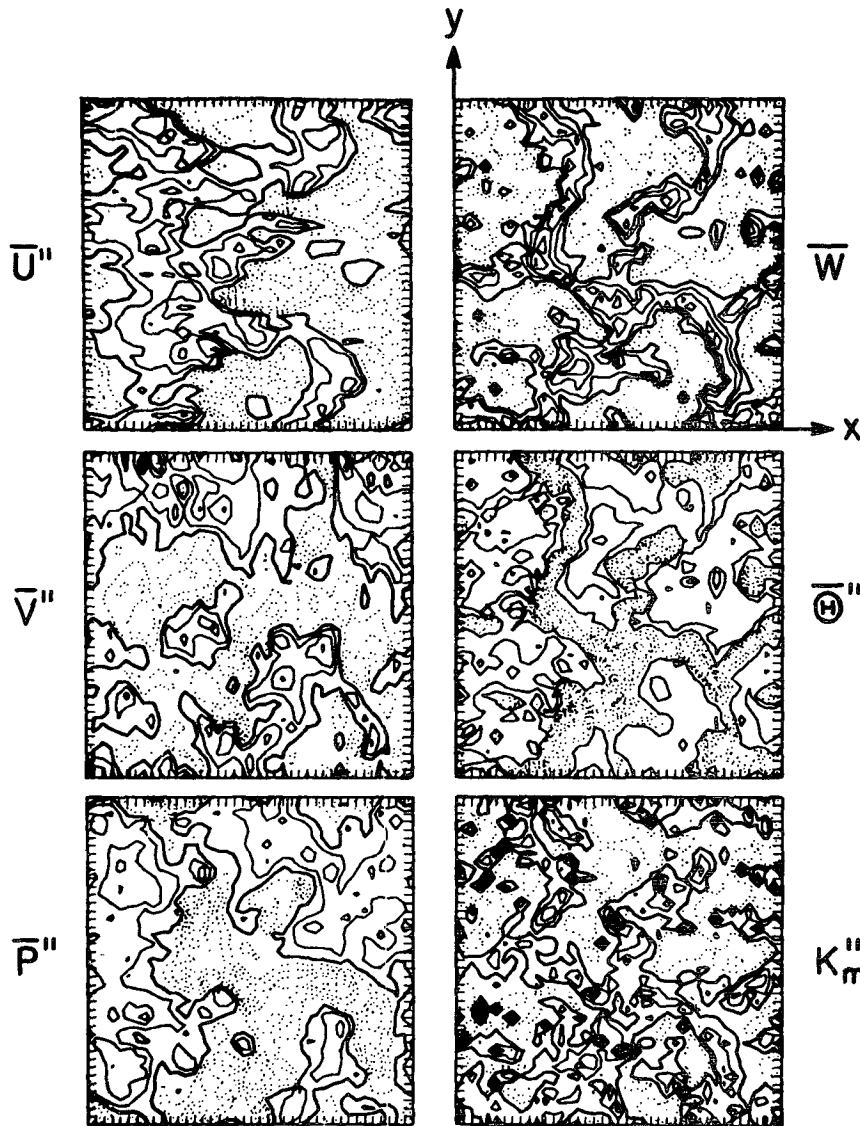


FIG. 22. Contour of u'' , w , v'' , θ'' , P'' and K_m'' in the x - y plane at $z=0.25$ at time $t=16.008$ for $-z_i/L=45$. Contour intervals are 1.25 for u'' and v'' , 2.0 for w , 0.15 for θ'' , 3.0 for P'' , and 0.004 for K_m'' . Other details are as described in the legend to Fig. 18.

The reliability of the "slope" statistic they calculated is not in doubt, however.

As $-z_i/L$ increases, Figs. 25-27 show that the tilts in \bar{v} and $\bar{\theta}$ are confined to smaller heights and are scarcely noticeable for $-z_i/L=45$. Acoustic measurements of thermal plumes by Beran *et al.* (1971) in unstable conditions tend to confirm the lack of tilt for heights above 30 m. However, careful examination of the original computer-drawn eddy contours shows that the tendency for warm air to be concentrated on the upstream edge of the thermal plumes [positive values of $\langle(\partial\theta/\partial x)^2\rangle$] persists to heights of at least $0.45z_i$ even for the case of $-z_i/L=45$ when the large-scale structure is randomly oriented at such a height.

Views in a y - z plane tended to show circulations

transporting momentum downward in this plane in preference to x - z planes, for $-z_i/L \leq 4.5$.

b. Merging of plumes

An example of the way new thermal elements are born, grow and merge into pre-existing large plumes extending to the top of the region modeled is shown in Fig. 28, which depicts the \bar{w} field in an x - z plane as a function of time for the case $-z_i/L=45$. The dimensionless time interval between views is 0.072, which corresponds to 3 min when $z_i=1$ km and $u_*=40$ cm sec⁻¹. Fig. 27 is for a time only 0.015 before Fig. 28b. Two plumes or updrafts of particular interest here have only recently appeared significant, and are located

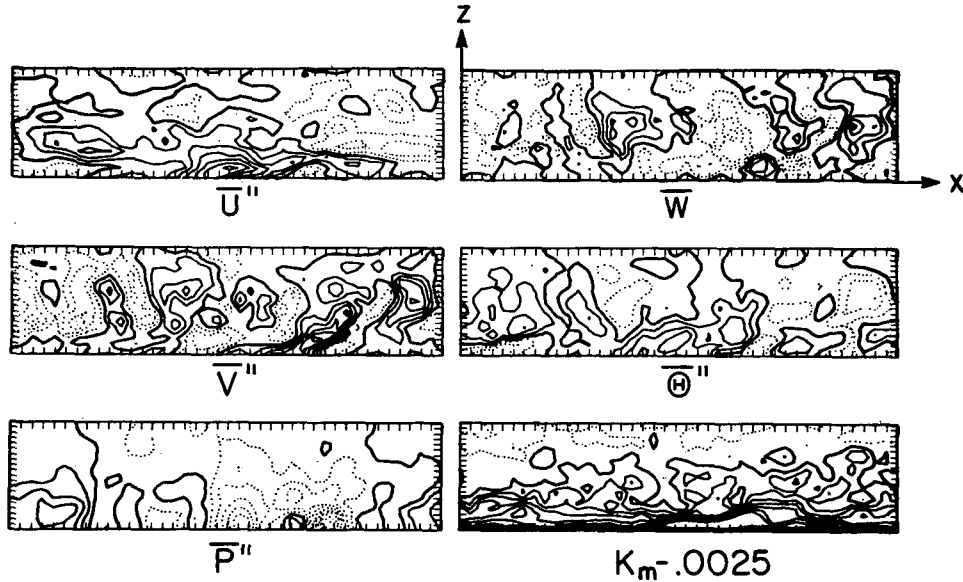


FIG. 23. Contours of $\bar{u}'', \bar{w}, \bar{v}'', \bar{\theta}'', \bar{p}''$ and $K_m - 0.0025$ in the x - z plane at $y = 5\Delta y$ at time $t = 11.125$ for the neutral case. The contour interval for K_m is 0.0010. Other details are as described in the legend to Fig. 18.

at $x = 26\Delta x$ and $28\Delta x$, respectively, out of $40\Delta x$ in Fig. 28a. They are accompanied by positive temperature anomalies, and are here called "plumes" because their bases remain in contact with the surface during growth. At this time the two new plumes, if viewed on a horizontal plane at a small height, would each appear as a warm anomaly on only a single grid point (producing an isolated diamond-shaped contour of which about 14 appear in Fig. 22 for \bar{w}). The ensuing growth of both plumes and eventual merger into, and dominance of, the giant plume on the right may be traced

in the figures. Another updraft centered at $x = 5\Delta x$ in Fig. 28a also grows swiftly and merges with a pre-existing updraft during Figs. 28d and e. Other changes not readily explained from these views occur because of lateral advection and vertical pressure gradients. From examination of these and other growing plumes, the length of time for a small but "successful" new updraft of height $0.1z_i$ to mature into a large one of height z_i is estimated to be $2.5z_i/w_*$.

Due to the continual amalgamation of growing plumes into more mature ones, the latter change shape

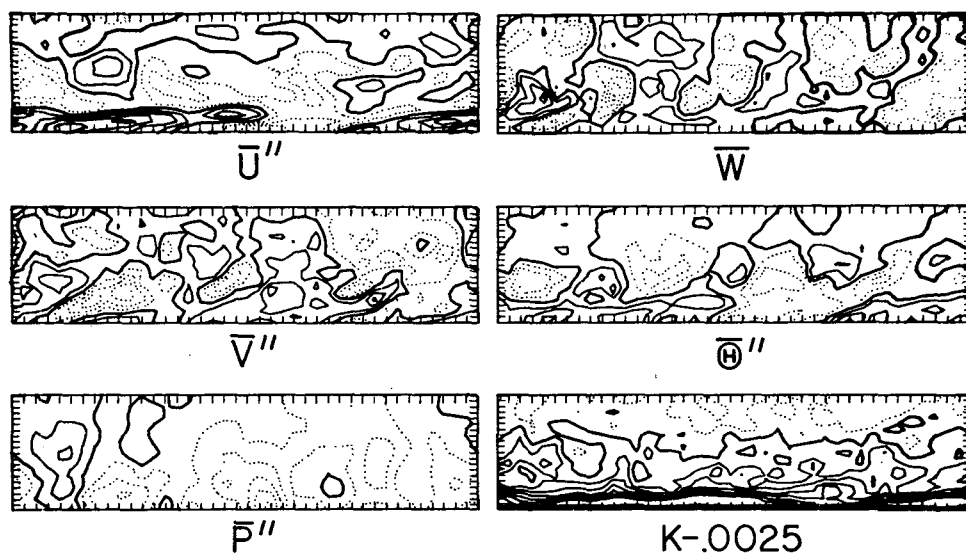


FIG. 24. Contours of $\bar{u}'', \bar{w}, \bar{v}'', \bar{\theta}'', \bar{p}''$ and $K_m - 0.0025$ in the x - z plane at $y = 5\Delta y$ at time $t = 10.750$ for the neutral case. The contour interval for K_m is 0.0010. Other details are as described in the legend to Fig. 18.

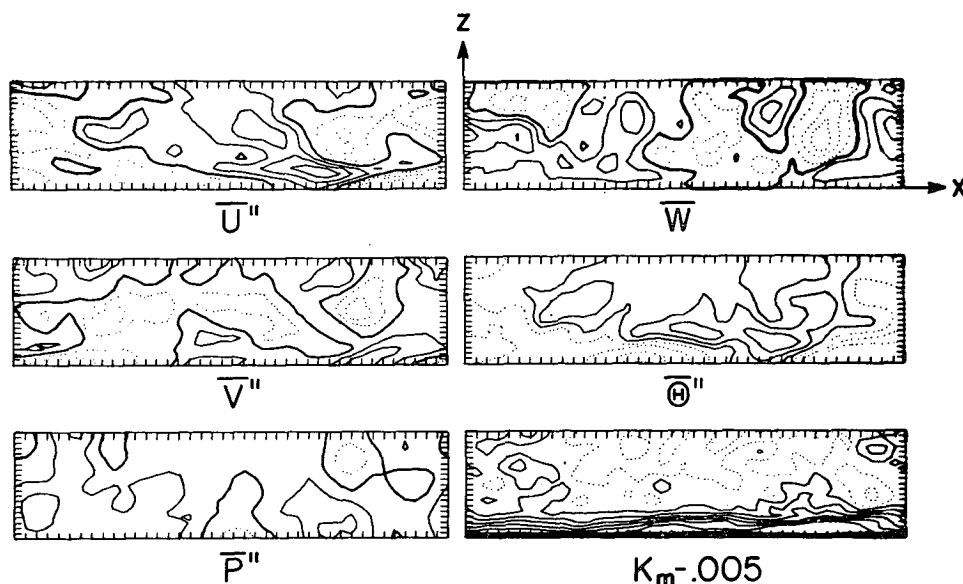


FIG. 25. Contours of \bar{u}'' , \bar{w} , \bar{v}'' , $\bar{\Theta}''$, \bar{P}'' and $K_m - 0.0050$ in the x - z plane at $y = 5\Delta y$ at time $t = 2.832$ for $-z_i/L = 1.5$. Contour intervals are 0.40 for $\bar{\Theta}''$ and 0.0016 for K_m . Other details are as described in the legend to Fig. 18.

from one configuration of the perimeter to a completely different one in a time scale of about $1.5z_i/w_*$. A particular center of updraft activity, however, has a much larger time scale as it drifts downwind. Because of the frequency and importance of plume mergers, inclusion of this mechanism into theories of convection plumes, such as that of Telford (1970), should be considered as the next major step to be taken toward increased

aerism. The importance of plume mergers in convective turbulence has been previously inferred by Vul'fson (1961).

These figures drawn by the computer help to suggest the wealth of information on the energy-containing eddies which can be tapped by the numerical approach in three dimensions, but which can only partially be presented here.

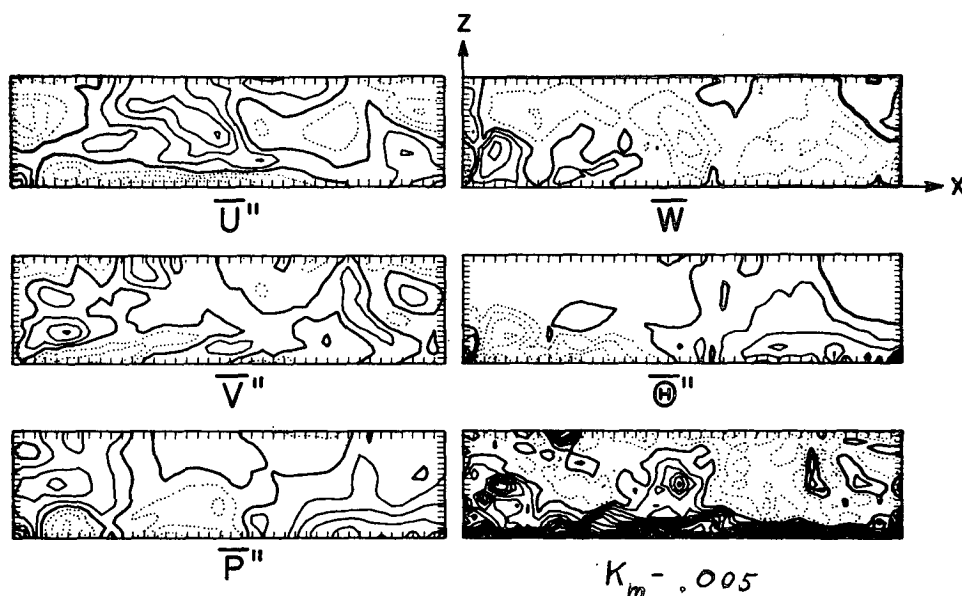


FIG. 26. Contours of \bar{u}'' , \bar{w} , \bar{v}'' , $\bar{\Theta}''$, \bar{P}'' and $K_m - 0.0050$ in the x - z plane at $y = 5\Delta y$ at time $t = 9.875$ for $-z_i/L = 4.5$. Contour intervals are 0.75 for \bar{w} , 0.38 for $\bar{\Theta}''$, and 0.0010 for K_m . Other details are as described in the legend to Fig. 18.

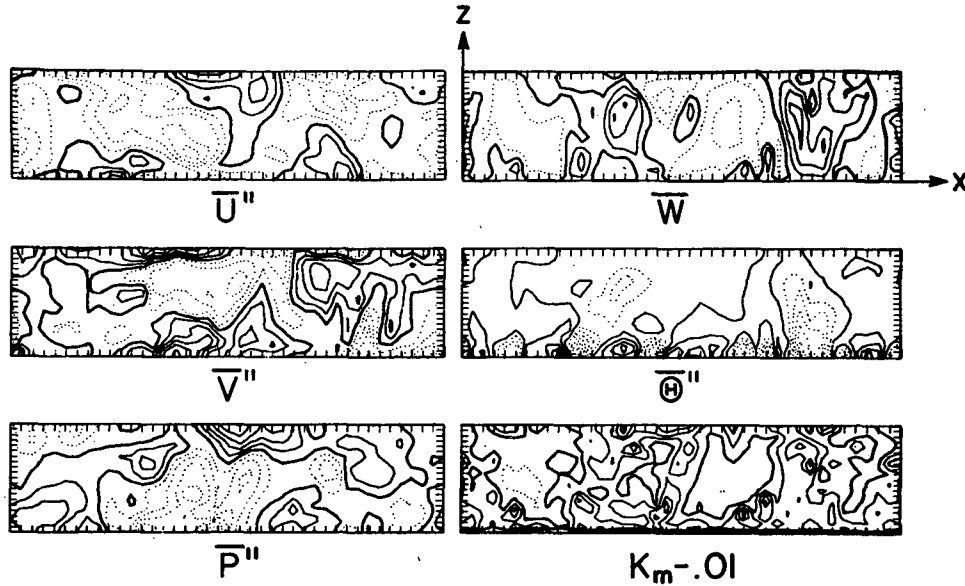


FIG. 27. Contours of \bar{u}'' , \bar{w} , \bar{v}'' , $\bar{\theta}''$, \bar{p}'' and $K_m - 0.010$ in the x - z plane at $y = 5\Delta y$ at time $t = 16.008$ for $-z_i/L = 45$. Contour intervals are as indicated in the legend to Fig. 22.

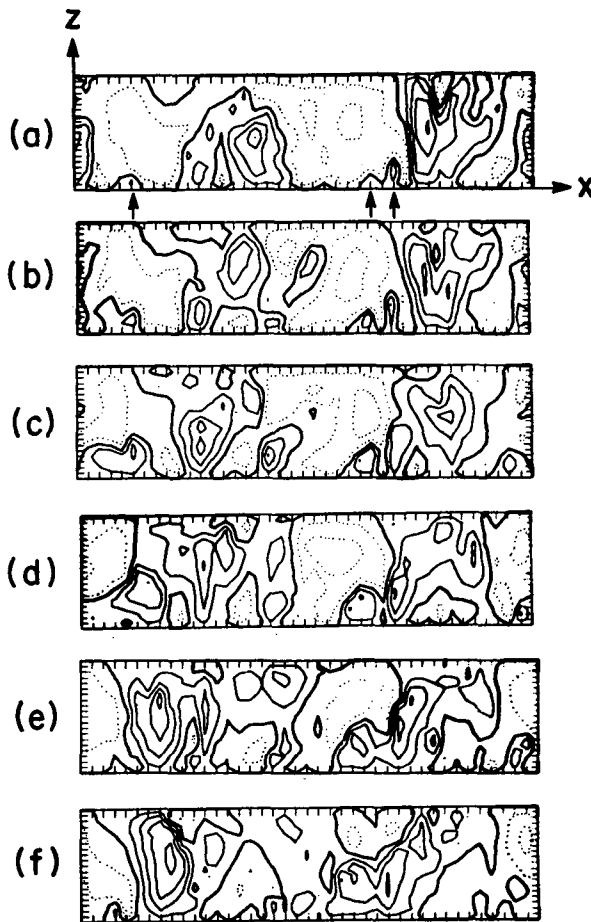


FIG. 28. Time sequence of contours of \bar{w} in the x - z plane at $y = 5\Delta y$ for $-z_i/L = 45$ for a contour interval of 2.0. Fig. 28(a): $t = 15.951$, arrows denote developing plumes discussed in text; Fig. 28(b): $t = 16.023$; Fig. 28(c): $t = 16.095$; Fig. 28(d): $t = 16.167$; Fig. 28(e): $t = 16.239$; Fig. 28(f): $t = 16.314$.

5. Dispersion of particles released instantaneously near the surface

Large numbers of particles initially existing at grid points on a given horizontal plane near the surface were subsequently advected using forward time steps. Each advecting velocity component was evaluated at the location of the particle by an interpolation utilizing 10 neighboring grid values. In addition, after each time step a random displacement (of uniform probability distribution) to simulate dispersion due to sub-grid-scale motions was applied to each particle. The rms SGS displacement at the end of each time step was prescribed to be $0.37(K_m \Delta t)^{1/2}$, and turned out to be small in comparison with the deterministic advective displacements above the lowest grid interval. Particles which were occasionally advected by the SGS displacements a given distance below $\hat{z} = 0$ or above $\hat{z} = z_i$ were reflected inward the same distance. The number of particles involved in each release was 800.

The mean height $\langle z_p \rangle$ of the particles as a function of dimensionless time after release is shown in Fig. 29 for three different thermal stabilities. In the neutral case, the time after release is made dimensionless on the lower abscissa by the ratio of the characteristic height of the neutral PBL ($0.35u_*/f$) and the friction velocity u_* , i.e., by $0.35/f$. In the unstable cases, time is made dimensionless by the analogous ratio z_i/u_* on the lower abscissa. For any given value of u_* , it is seen that a much greater time is necessary to disperse particles well into the neutral PBL than into a thermally unstable PBL. In fact, the numerical integration for the neutral case did not last nearly long enough for the particles to become well mixed (for which $\langle \hat{z}_p \rangle$ would equal about $0.17 u_*/f$ or more). It is estimated from the figure that the time for this to occur would

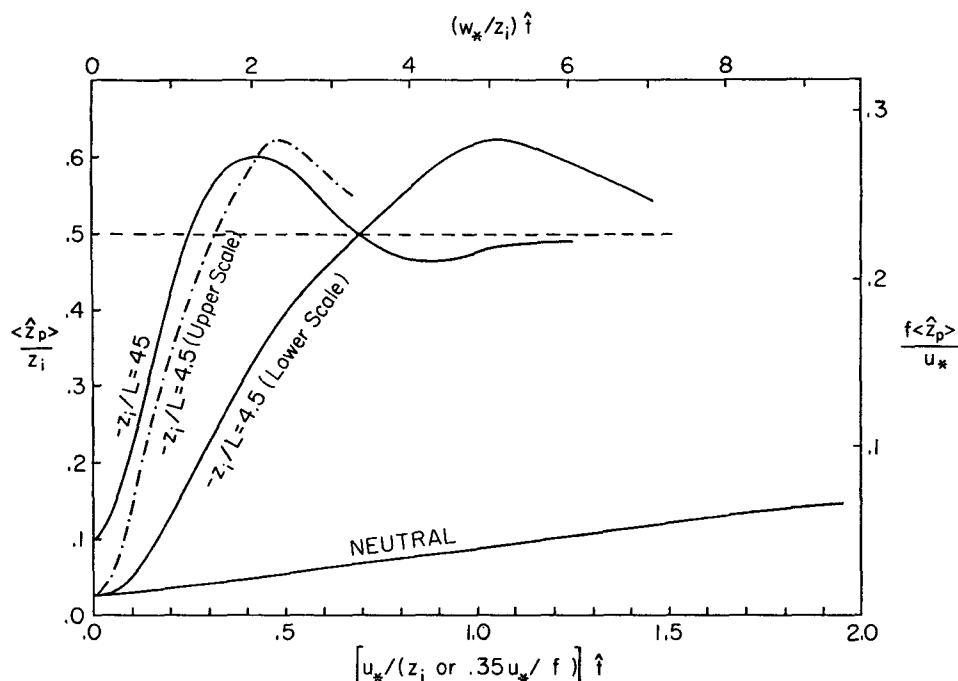


FIG. 29. Dimensionless mean height of 800 nonbuoyant particles released simultaneously from an x - y plane near the surface, as a function of the dimensionless time after release. In the neutral case the right-hand ordinate applies, as does the lower abscissa for which time is made dimensionless by $0.35/f$. In unstable cases the left-hand ordinate applies, while the lower abscissa pertains to the solid curves with time made dimensionless by u_*/z_i . The upper abscissa applies to $-z_i/L=45$ and to the dash-dot curve, with time after release then made dimensionless by z_i/w_* .

be in excess of $3/f$, which is typically of the order of 8 hr. The slope of $\langle \hat{z}_p \rangle$ vs time in the nearly linear region corresponds to $d\langle \hat{z}_p \rangle/d\hat{t} = 0.09u_*$.

In the unstable cases, thorough mixing occurred relatively quickly, and was aided by the fact that the particles overshot the final equilibrium height of $0.5z_i$ before gradually approaching this height from above. The upper abscissa in Fig. 29 is the PBL free-convection scale which is seen to bring both unstable cases into near agreement, especially upon allowing for the fact that the particles in the case $-z_i/L=45$ were released at $0.10z_i$ instead of at $0.025z_i$. Hence, the time for particles released near the surface, in a moderately or highly unstable PBL, to first reach $\langle \hat{z}_p \rangle = 0.5z_i$ is here found to be about $1.6z_i/w_*$, which is characteristically only about 15 min. The effectiveness of vertical mixing in the unstable PBL is thus seen to be one or two orders of magnitude greater than that of the neutral PBL. Part of the increased effectiveness is caused by the greater amplitude of the vertical motions in the unstable case, but much is also due to the greater Lagrangian time scale for vertical velocity. Whatever the horizontal location of a released particle, it was found to become incorporated within an updraft in a relatively short time; and more likely than not to continue traveling upward past $\hat{z}=0.5z_i$ before turning downward.

The rms vertical spread of the particles about the release level was also calculated. This quantity was

generally found to be about $1.25\langle \hat{z}_p \rangle$ for $0.1 < \langle \hat{z}_p \rangle < 0.4$. This value is to be expected if the vertical distribution were half-Gaussian with peak concentration and release level located at $z=0$.

6. Conclusions and outlook

Seven of the more important conclusions are listed in Section 1; others are located throughout Sections 3–5. Still others were not presented due to lack of space. Conclusions concerning the upper portion of the PBL were either not drawn or not emphasized because of the influence of the incorrect upper boundary conditions utilized. Similarly, velocity and temperature variances and certain other statistics at the lowest one or two grid levels were not considered very accurate because of the large contributions from sub-grid-scale motions which must be supplied by assumption. Fortunately, the results calculated for resolvable scales stand independent of whatever assumptions are made for the SGS variances in velocity and temperature. As applied to the energy-containing eddies of scale between $0.2h$ and $4h$ in the lower half or two-thirds of the PBL, the results are therefore believed to be essentially valid for conditions of equilibrium and horizontal homogeneity of mean velocity, mean temperature, mean horizontal pressure gradient, and surface roughness; and for unsaturated air.

The results contained herein represent about 150 hr

of machine time and auxiliary-equipment time distributed over $1\frac{1}{2}$ years on the CDC 6600 computer of the National Center for Atmospheric Research. Over half this time was spent in reaching the statistically steady state, starting in the four cases from initial conditions characteristic of some other state. The rest was spent in generating the various realizations which made up the ensembles producing the statistics. A modest increase of computer speed, if accompanied by a corresponding increase in size of readily accessible computer memory, would allow the entrainment process at the top of the unstable PBL to be modeled in three dimensions, along with the imposition of a lid at a higher level above the PBL. It would also allow the addition of water vapor, so that the separate influences of vapor and temperature upon the virtual potential temperature could be examined.

In order that calculations such as these be extended to cover mesoscale motions within a grid area of an atmospheric circulation model, of say 100 km on a side, the number of grid intervals would have to be increased by a factor of about 625. This appears to be out of the question in the next few decades, unless requirements were relaxed by increasing the grid size of the three-dimensional model. However, this step is not recommended here because the vertical velocity, which transports heat, momentum and kinetic energy, has most of its energy concentrated on horizontal scales comparable to the height of the PBL above the surface layer. Therefore, if the horizontal grid interval were increased from $0.1h$ to h , for example, the assumptions for the SGS eddy coefficient would become crucial at all levels in the PBL, not just at the lowest one or two levels. Furthermore, the assumption of Reynolds stress proportional to velocity deformation through a scalar eddy coefficient would then probably become untenable. Instead, it is recommended, if more computer power becomes available, that the horizontal grid scale be made smaller and the area modeled larger than the values used in this study. This recommendation is most reasonable under conditions for which a spectral gap, between mesoscale and PBL-scale motions, exists on scales of from 5–10 km.

Acknowledgments. I am indebted to F. Lipps of the Geophysical Fluid Dynamics Laboratory, Princeton, for explanation and use of his fast-Fourier transform/matrix-inversion method for exact solution of the Poisson equation for pressure; to P. Rotar, D. Kitts, J. Adams, D. Robertson, R. Jenne and D. Joseph, of the NCAR Computing Facility, for helping me overcome certain programming and tape-reading problems; to D. K. Lilly for helpful discussions on Ekman instability and for suggested improvements in the manuscript; to D. Lenschow for discussions of aircraft measurements in the planetary boundary layer; to J. W. Telford for a discussion on the use of virtual potential temperature; and to H. Tennekes for incentive to

study the depth of the momentum boundary layer in the weakly unstable case.

REFERENCES

- Angell, J. K., 1971: Helical circulations in the planetary boundary layer. *J. Atmos. Sci.*, **28**, 135–138.
- , D. H. Pack and C. R. Dickson, 1968: A Lagrangian study of helical circulations in the planetary boundary layer. *J. Atmos. Sci.*, **25**, 707–717.
- Beran, D. W., C. G. Little and B. C. Willmarth, 1971: Acoustic Doppler measurements of vertical velocities in the atmosphere. *Nature*, **230**, 160–162.
- Businger, J. A., 1966: Transfer of momentum and heat in the planetary boundary layer. *Proc. Symp. Arctic Heat Budget and Atmos. Circulation*, RM-5233-NSF, Rand Corp., 305–322.
- , J. C. Wyngaard, Y. Izumi and E. F. Bradley, 1971: Flux-profile relationships in the atmospheric surface layer. *J. Atmos. Sci.*, **28**, 181–189.
- Clarke, R. H., 1970: Observational studies in the atmospheric boundary layer. *Quart. J. Roy. Meteor. Soc.*, **96**, 91–114.
- Crow, S. C., 1968: Viscoelastic properties of fine-grained incompressible turbulence. *J. Fluid Mech.*, **33**, 1–20.
- Deardorff, J. W., 1970a: A three-dimensional numerical investigation of the idealized planetary boundary layer. *Geophys. Fluid Dyn.*, **1**, 377–410.
- , 1970b: Preliminary results from numerical integrations of the unstable planetary boundary layer. *J. Atmos. Sci.*, **27**, 1209–1211.
- , 1970c: Convective velocity and temperature scales for the unstable planetary boundary layer and for Rayleigh convection. *J. Atmos. Sci.*, **27**, 1211–1213.
- , 1970d: A numerical study of three-dimensional turbulent channel flow at large Reynolds numbers. *J. Fluid Mech.*, **41**, 453–480.
- , 1971: On the magnitude of the subgrid scale eddy coefficient. *J. Comput. Phys.*, **1**, 120–133.
- , G. E. Willis and D. K. Lilly, 1969: Laboratory investigation of nonsteady penetrative convection. *J. Fluid Mech.*, **35**, 7–31.
- Dyer, A. J., 1967: The turbulent transport of heat and water vapor in an unstable atmosphere. *Quart. J. Roy. Meteor. Soc.*, **93**, 501–508.
- Faller, A. J., and R. E. Kaylor, 1966: A numerical study of the instability of the laminar Ekman boundary layer. *J. Atmos. Sci.*, **23**, 466–480.
- Harlow, F. H., and J. E. Welch, 1965: Numerical calculation of time-dependent viscous incompressible flow of fluid with free surface. *Phys. Fluids*, **8**, 2182–2189.
- Haugen, D. A., J. C. Kaimal and E. F. Bradley, 1971: An experimental study of Reynolds stress and heat flux in the atmospheric surface layer. *Quart. J. Roy. Meteor. Soc.*, **97**, 168–180.
- Kuettner, J. P., 1971: Cloud bands in the earth's atmosphere. Submitted to *Tellus*.
- Konrad, T. G., 1968: The alignment of clear-air convective cells. *Proc. Intern. Conf. Cloud Physics*, Toronto, Canada.
- Lavoie, R. L., R. W. Cotton and J. B. Hovemale, 1970: Investigations of lake-effect storms. Final Rept., Contract E22-103-68(N), Dept. of Meteorology, The Pennsylvania State University, 127 pp.
- Lenschow, D. H., 1970: Airplane measurements of planetary boundary layer structure. *J. Appl. Meteor.*, **9**, 874–884.
- Lilly, D. K., 1965: On the computational stability of numerical solutions of time-dependent non-linear geophysical fluid dynamics problems. *Mon. Wea. Rev.*, **93**, 11–26.
- , 1966: On the instability of Ekman boundary flow. *J. Atmos. Sci.*, **23**, 481–494.
- , 1967: The representation of small-scale turbulence in numerical simulation experiments. *Proc. IBM Sci. Computing Symp. Environmental Sci.*, IBM Form No. 320-1951, 195–210.

- , 1968: Models of cloud-topped mixed layers under a strong inversion. *Quart. J. Roy. Meteor. Soc.*, **94**, 292–309.
- Monin, A. S., 1970: The atmospheric boundary layer. *Annual Reviews of Fluid Mechanics*, Palo Alto, Calif. Annual Reviews, Inc., 225–250.
- Myrup, L. O., 1967: Temperature and vertical velocity fluctuations in strong convection. *Quart. J. Roy. Meteor. Soc.*, **93**, 350–360.
- Orszag, S. A., 1971: Numerical simulation of incompressible flows within simple boundaries. II. Accuracy. To appear in *J. Fluid Mech.*
- Pielke, R. A., and H. A. Panofsky, 1970: Turbulence characteristics along several towers. *Boundary-Layer Meteor.*, **1**, 115–130.
- Priestly, C. H. B., 1954: Convection from a large horizontal surface. *Australian J. Phys.*, **7**, 176–201.
- Smagorinsky, J., 1963: General circulation experiments with the primitive equations: 1. The basic experiment. *Mon. Wea. Rev.*, **91**, 99–164.
- Smith, S. D., E. G. Banke and O. M. Johannessen, 1970: Wind stress and turbulence over ice in the gulf of St. Lawrence. *J. Geophys. Res.*, **75**, 2803–2812.
- Telford, J. W., 1970: Convective plumes in a convective field. *J. Atmos. Sci.*, **27**, 347–358.
- , and J. Warner, 1964: Fluxes of heat and vapor in the lower atmosphere derived from aircraft observations. *J. Atmos. Sci.*, **21**, 539–548.
- Tennekes, H., 1970: Free convection in the turbulent Ekman layer of the atmosphere. *J. Atmos. Sci.*, **27**, 1027–1034.
- , 1971: Reply to “Comments on free convection in the turbulent Ekman layer of the atmosphere.” *J. Atmos. Sci.*, **28**, 300–301.
- Vul’fson, N. L., 1961: *Convective Motions in a Free Atmosphere*. Israel Program for Scientific Translations Ltd., 188 pp.
- Webb, E. K., 1970: Profile relationships: The log-linear range and extension to strong stability. *Quart. J. Roy. Meteor. Soc.*, **96**, 67–90.
- Weiler, H. S., and R. W. Burling, 1967: Direct measurements of stress and spectra of turbulence in the boundary layer over the sea. *J. Atmos. Sci.*, **24**, 653–664.
- Williams, G. P., 1969: Numerical integration of the three-dimensional Navier-Stokes equations for incompressible flow. *J. Fluid Mech.*, **37**, 727–750.
- Wyngaard, J. C., O. R. Coté and Y. Izumi, 1971: Local free convection, similarity, and the budgets of shear stress and heat flux. *J. Atmos. Sci.*, **28**, 1171–1182.
- Zubkovskiy, S. L., and B. M. Koprov, 1970: On the turbulent energy balance in the boundary layer of the atmosphere. *Izv. Atmos. Oceanic Phys.*, **6**, 989–995.